Manuscript

# Application of airborne, laboratory and field hyperspectral methods to mineral exploration in the Canadian Arctic: recognition and characterization of volcanogenic massive sulfide-associated hydrothermal alteration in the Izok Lake deposit area, Nunavut, Canada

By

K. Laakso[a*], B. Rivard[a], J.M. Peter[b], H.P. White[c], M. Maloley[c], J. Harris[b] and D. Rogge[d]

[a]Center for Earth Observation Science, Department of Earth and Atmospheric Sciences, University of Alberta, 1-26 Earth Sciences Building, University of Alberta, Edmonton, Alberta, Canada, T6G 2E3
[b]Geological Survey of Canada, Booth Street 601, Ottawa, Ontario, Canada, K1A 0E8
[c]Canada Centre for Remote Sensing, 6-A19 – 560 Rochester Street, Ottawa, Ontario, Canada, K1A 0E4
[d]German Aerospace Center (DLR) Oberpfaffenhofen, Münchener Straße 20, 82234 Weßling, Germany

[*]Corresponding author. Tel.: +358 40 7326672. E-mail: laakso@ualberta.ca

September 28th 2014

**Abstract:** We have investigated the application of ground, laboratory and airborne optical remote sensing methods for the detection of hydrothermal alteration zones associated with volcanogenic massive sulfide (VMS) deposits. We use the Izok Lake deposit in Nunavut, Canada as a test case. This bimodal-felsic Zn-Cu-Pb-Ag deposit is located above the tree line in a subarctic environment where lichens are the dominant cryptogamic species coating the rocks. The immediate host rhyolitic rocks have been hydrothermally altered and contain biotite, chlorite and white micas as dominant alteration minerals. These minerals have spectral Al-OH and Fe-OH absorption features in the short-wave infrared wavelength region that display wavelength shifts, which are documented to be due to chemical compositional changes. Our ground hyperspectral results indicate that there is a systematic trend in the Fe-OH absorption feature wavelength position of biotite/chlorite with increasing distance from the VMS deposit: the average Fe-OH absorption feature wavelength position of the proximal areas (398-3146 m from mineralization) is observed at 2254 nm, and that of the distal areas (5782-6812 m) at 2251 nm. Moreover, the proximal areas have an average Al-OH absorption feature wavelength position at 2203 nm, in contrast with the average wavelength position at 2201 nm in the distal areas, implying a spectral shift of 2 nm. These findings indicate that hydrothermal alteration zones can be detected by hyperspectral remote sensing, despite the presence of abundant lichen cover. However, the airborne results discussed in this study required the screening out of more than 99% of the pixels in the area.

## 1. Introduction

Volcanogenic massive sulfide (VMS) deposits are economically important sources of Zn, Cu, Pb, Ag, and Au (Galley et al., 2007). These deposits form from hydrothermal fluids (downdrawn and modified seawater) that circulate and are heated by magmas in the subsurface, dissolve metals and other solutes in the rocks along the flow

path, and vent at the seafloor. The varying temperature and chemical gradients of the fluids along their circulation path result in a range of chemical, mineralogical and textural compositional changes in the host rocks. The extent and magnitude of these changes are determined by physico-chemical factors such as the temperature, pH, water/rock ratios, $fO_2$, $fS_2$, as well as the composition of the hydrothermal fluids and the host rocks.

The mineralogical assemblages that develop through hydrothermal alteration in different VMS deposits vary, but phyllosilicate minerals such as chlorite and sericite (fine-grained micaceous minerals, Eberl et al., 1987) are typically present. The phyllosilicates that form through hydrothermal alteration can have variable chemical compositions (e.g., muscovite, paragonite, phengite, celadonite, Fe-chlorite and Mg-chlorite) within a VMS system due to different physico-chemical conditions in different parts of the system. High temperatures are favorable for the formation of Al-rich muscovite and Fe-rich chlorite and biotite (Miyashiro and Shido, 1985; Cathelineau, 1988; Duke, 1994). Factors such as the chemical composition of the hydrothermal fluids and the host rocks may simultaneously influence the composition of the developing mineral assemblages (Kranidiotis and MacLean, 1987; Cathelineau, 1988; Van Ruitenbeek et al., 2005). The chemical composition of the phyllosilicate minerals may change through several substitutions such as simple Mg-Fe substitution or Tschermak substitution, in which octahedral Mg and Fe substitute for Al concurrently with tetrahedral Si for Al (Miyashiro and Shido, 1985; Guidotti and Sassi, 1998).

The short-wave infrared (SWIR, 1300-2500 nm) spectrometric response of the phyllosilicate minerals is sensitive to the cation substitutions discussed above. These substitutions can be observed as spectral shifts within the Al-OH and Fe-OH absorption features near 2200 nm and 2250 nm, respectively (Clark et al., 2007). The wavelength position of the Al-OH absorption feature, present in dioctahedral muscovite, shifts

systematically toward shorter wavelengths as the Al content of the octahedral sites increases, and the opposite effect, or a systematic shift toward longer wavelengths, takes place when the relative proportion of octahedral Mg and Fe increase (Post and Noble, 1993; Duke, 1994). These dioctahedral minerals form a solid solution series between paragonite, muscovite and phengite (Velde 1965, Li et al., 1994) and are commonly termed white micas. Similar to white micas, the Fe-OH absorption feature that is present in biotite and chlorite (Scott and Yang, 1997), shifts toward shorter wavelengths with increasing Mg content, and toward longer wavelengths with increasing Fe content (Bassett, 1960; McLeod et al., 1987).

Previously, the wavelength positions of the Al-OH and Fe-OH absorption features extracted from laboratory hyperspectral data were used to delineate the alteration zones of the Myra Falls VMS deposit in British Columbia (Jones et al., 2005) and the Boco VMS Prospect in Tasmania, Australia (Herrmann et al., 2009). Van Ruitenbeek et al. (2006) mapped the Al-OH absorption feature wavelength positions of the Panorama VMS district, Soansville greenstone belt, Pilbara region, Australia, by using spectral ratios extracted from hyperspectral airborne data. These studies show that the spectral shifts of the Al-OH and Fe-OH absorption feature wavelength positions can be detected by hyperspectral remote sensing in VMS deposit environments and that these shifts are associated with chemical compositional variations of the phyllosilicate minerals. However, the application of hyperspectral airborne data for mapping the Al-OH and Fe-OH absorption feature wavelength positions of phyllosilicate minerals has not previously been demonstrated in high latitude environments that typically have abundant lichen cover on rock outcrops. Lichens are the dominant autotrophs of many subpolar ecosystems due to their ability to withstand extreme environmental conditions (Longton, 1988; Purvis, 2000). Lichens are also optically thick, and hence can hinder the detection of spectral features of rock substrates (e.g., Ager and Milton, 1987; Rivard and

Arvidson, 1992; Bechtel et al. 2002).

The present study was conducted in the Point Lake greenstone belt, in the area that hosts the Izok Lake (65° 38'N, 112 48'W in Nunavut, Canada) Zn-Cu-Pb-Ag VMS deposit. The salient objective was to determine if the distribution of hydrothermally altered rocks associated with the deposit could be mapped using hyperspectral remote sensing data and processing methods, in the presence of abundant lichens on the rock outcrops. This objective was addressed by examining the Al-OH and Fe-OH absorption feature wavelengths positions of white micas and biotite/chlorite. These absorption feature wavelength positions were examined using various levels of spectroscopic data that were related to the mineralogy of the study area and distance from mineralization.

## 2. Study Area

The study area is in the Kitikmeot region of Nunavut, northern Canada (Fig. 1). The area comprises 15.5 $km^2$ of gently rolling bedrock hills that are interrupted by more prominent ridges. It also hosts numerous ponds and lakes. The nearest weather station to provide long-term climatological data is located in Lupin (weather station "Lupin A", 65°45' N , 111°15' W), 72 km NE of Izok Lake. According to this weather station, the daily average temperature is -10.9 °C between 1982 and 2006 (Government of Canada, 2014). The Kitikmeot region is characterized by Arctic tundra vegetation that is dominated by shrubs, sedges, grasses and flowering herbs (Laidler et al., 2008). Lichens are abundant on many outcrops in the Izok Lake area, and typically cover 75-100% of the rock surfaces.

The study area is underlain by the Point Lake Formation of the Yellowknife Supergroup, which is part of the Slave structural province (Bostock, 1980). The massive sulfide lenses of the Izok Lake deposit are predominantly hosted by Archean (2.6 Ga; Mortensen et al., 1988) rhyolitic rocks and, to a lesser extent, by intermediate to mafic metavolcanic and metasedimentary rocks. These rhyolitic rocks contain white mica,

biotite and chlorite some of which formed as the result of hydrothermal alteration that occurred during massive sulfide emplacement (Morrison, 2004). The original alteration minerals have been metamorphosed to pyroxene hornfels facies conditions that have induced both textural and mineralogical changes. Porphyroblastic textures predominate and minerals such as anthophyllite and cordierite occur in places (Morrison, 2004). Despite metamorphism, the primary alteration assemblages are largely preserved in the stratigraphic hanging wall and footwall of the deposit, and this serves as the rationale for evaluating the application of hyperspectral methods for detecting this hydrothermal alteration in the exploration for VMS mineralization.

## 3. Spectral datasets

### *3.1 Ground site selection and spectral measurements*

Several sub-areas were selected strategically within the study area for the acquisition of ground spectrometry with the aim of recognizing and delineating any hydrothermal alteration zones associated with the Izok Lake deposit. These sites encompass the intensely altered areas proximal to mineralization, and less altered areas distal from the massive sulfides. An estimate of the intensity of alteration throughout the study area was obtained by using the bulk rock $Na_2O$ isopleth map of Morrison (2004; Fig. 1). Sodium depletion results from the breakdown of sodic plagioclase during hydrothermal alteration, and is a reliable indicator of hydrothermal alteration intensity. Areas of both intense and weak alteration were targeted to reveal possible trends in the chemical compositions of the phyllosilicate minerals by collection and analysis of 285 spectra from the areas of intense alteration and 170 spectra from less intensely altered areas. In total, 455 spectral measurements were collected from 108 rhyolitic rock outcrops over two field seasons (2010 and 2013). At each measurement site, one to eight spectral measurements, each with a 1 cm diameter circular footprint, were collected

from the lichen-free and weathered surfaces of each rock outcrop. These measurements were collected randomly from an area of approximately 0.25 $m^2$ per rock outcrop. All the measurements were collected from the horizontal surfaces of the rock outcrops to ensure optimal comparability of the ground and airborne spectra. In the field, visual inspection of the rock outcrops, combined with knowledge of the geology of the study area (see Fig. 1), were used to ensure that spectral measurements were obtained only from rhyolitic rock outcrops. Some of the rhyolitic outcrops were stripped of lichens and surficial material by Minerals and Metals Group (MMG; the owner of the deposit) personnel with the use of a pressure washer, and these rock outcrops were preferred for spectral measurements over non-pressure washed outcrops because they are devoid of lichens. The solution used for pressure washing was water from the lakes of the study area. Undisturbed, natural (i.e. non-pressure washed), rhyolitic outcrops have variable lichen cover that ranges from sparse (covering 0-25% of the surface area) to abundant (covering 75-100% of the surface area). Examples of pressure-washed and lichen-covered rock outcrops are shown in Figures 2A,B.

All spectral measurements were made with a PANalytical Boulder Inc. (formerly ASD Inc.) FieldSpec® 3 (hereafter referred to as ASD) spectrometer that records spectra in the 350-2500 nm wavelength range with a spectral resolution of 10 nm and a sampling interval of 1 nm in the SWIR wavelength region. All measurements were obtained using a contact probe that has an internal illumination source that ensures consistent illumination conditions during data acquisition. Radiance values were converted to reflectance values by means of a Spectralon™ reflectance panel (i.e. the "white reference", SRT-99-100, Labsphere, Inc., North Sutton, NH, USA), a commercially available plate made of polytetrafluoroethylene (Bruegge et al., 1993). These relative reflectance values were converted to absolute reflectance values by multiplying the relative reflectance value of each wavelength with the reflectance factor

obtained from the calibration certificate of the Spectralon™ panel. This correction was conducted in accordance with the procedure suggested by Clark et al. (2002). The correction is necessary because the Spectralon™ panel has an absorption feature near 2130 nm (Clark et al., 2002). Dark current and white reference measurements were repeated every ten minutes during data acquisition in order to ensure consistency in the spectral measurements. The geographic coordinates of the rock outcrops were recorded using a handheld GPS, and all spectral measurements were acquired within a five meter radius from the X,Y co-ordinates recorded using the GPS. Each spectrum acquired in the field consists of 60 individual measurements taken consecutively and averaged by the ASD instrument.

*3.2 Sample suite and laboratory spectral measurements*

A hand specimen sample was collected from each of 60 rock outcrops that represent 65% of the 108 rhyolitic rock outcrops visited during the field works in 2010 and 2013. The aim was to collect samples both from the intensely altered and less altered parts of the study area. The bulk rock $Na_2O$ content isopleth map of Morrison (2004, Fig. 1) was used to guide the selection of the ground spectrometry sample locations; 39 samples were collected from the intensely altered areas, and 21 samples were collected from the less/least intensely altered parts of the study area. All samples collected have at least one weathered surface and sparsely lichen covered outcrops were preferentially sampled.

One to six spectral measurements were obtained in the laboratory from the weathered, lichen-free surfaces of each sample using an ASD FieldSpec® 3. If there were no weathered surfaces available, measurements were made on fresh surfaces. Reflectance spectra were acquired following the method described for ground

spectrometry, except that each spectrum acquired in the laboratory is the average of 25 individual consecutive measurements.

*3.3 Airborne spectral imaging*

Airborne hyperspectral data were collected over a 94 $km^2$ area comprising 58 flightlines within the Point Lake greenstone belt and centered on the Izok Lake deposit area during the period August 2-21, 2010. The data were acquired by SpecTIR LLC of Reno, Nevada using the ProSpecTIR® (AISA dual) sensor at a one meter spatial resolution. This sensor collects data in a nominal spectral resolution of 5 nm between 390 to 2500 nm. These data were resampled to a 6.3 nm interval, resulting in 360 channels.

The airborne dataset was pre-processed by SpecTIR by first converting the radiance data to reflectance data using the ATCOR-4® software package and MODTRAN® 4 atmospheric lookup tables (Richter and Schläpfer, 2002). Next, the dataset was geocorrected using the data extracted from a three-axis gyroscope attitude INS (Inertial Navigation System) that was positioned with a 12-channel GPS system and boresight calibration data. The data quality was confirmed by the Canada Centre for Remote Sensing using the Imaging Spectrometer Data Analysis System (ISDAS) package as outlined in Hitchcock and White (2007).

## 4. Petrography and Mineral Chemistry

Polished thin sections (PTS) were prepared from thirteen hand samples collected from outcrops during ground spectrometry collection (27, 29, 31, 34, 35, 37, 47, 51, 53, 54, 55, 56 and 59). These samples were chosen because their spectra have either an Al-OH or an Fe-OH absorption feature, which indicates the presence of white mica, biotite and chlorite. The PTS of samples 51, 53, 54, 55, 56 and 59 (geographic locations shown

in Fig. 1) were examined under a Nikon Labophot2® polarizing light microscope and the presence or absence of biotite, chlorite and muscovite was recorded at over 500 random spots within each PTS.

Next, seven samples (27, 29, 31, 34, 35, 37, 47) were selected for electron microprobe analysis (EMPA) based on the short, intermediate and long wavelength positions of their Al-OH and Fe-OH absorption features. Between 4 and 7 areas were selected within each PTS for analysis of white mica, biotite and chlorite. The PTS were carbon-coated and analyzed using a JEOL 8230 SuperProbe® electron microprobe operating at 20kV and using a beam current of 20 nA. Mineral formulae were calculated on the basis of 22 oxygens for micas (white micas and biotite) and 28 oxygens for chlorite. The results were compared to the spectral characteristics of these minerals by calculating the Pearson correlation coefficient between the Al-OH and Fe-OH wavelength positions and the Al, Fe, Mg and Si contents of white micas, biotite and chlorite, as determined by EMPA. These cations were chosen because their relative proportions in the octahedral sites of the phyllosilicate minerals determine the wavelength positions of the Al-OH and Fe-OH absorption features (Bassett, 1960; McLeod et al., 1987; Duke, 1994). In practice, we used the average compositions of these cations within each mineral (white mica and biotite/chlorite) for each sample (PTS). These average mineral cation compositions were then compared to the average Al-OH and Fe-OH absorption feature wavelength positions of the same samples from which the PTS were prepared. Sample 29 does not display clear Al-OH absorption features, and hence the average Al-OH absorption feature wavelength position of this sample is not compared to its chemical composition.

## 5. Spectral Analysis Methodologies

### *5.1 Ground and hand sample spectral processing*

Of the 455 spectral measurements acquired in the field, forty were discarded because of low signal-to-noise ratios or failed readings. The Al-OH and Fe-OH absorption feature wavelength positions of the remaining hull quotient-corrected spectra were manually extracted to discern the spectral shifts associated with the areas of hydrothermal altered rock. Hull quotient correction is conducted to reduce the effects of the background spectral slope when the absorption feature wavelength is to be accurately recorded (Clark and Roush, 1984). In practice, the hull quotient correction (continuum removal) is conducted by fitting straight-line segments (convex hull points) over the shoulders (maxima) of an absorption feature, and dividing the reflectance values of the absorption feature by these convex hull points. The resulting hull quotient values are normalized to a 0-1 scale hence removing the effects of albedo variance in the spectrum. An average wavelength position was then computed from the spectral measurements. In practice, this was achieved by conducting continuum removal and recording the minimum (the smallest hull quotient value) of each spectrum. These values were next averaged per rock outcrop. This averaging resulted in 98 Al-OH and 85 Fe-OH absorption feature wavelength position observations. In the case of the hand specimen samples, from one to six measurements per sample of the Al-OH and Fe-OH absorption feature wavelength positions were averaged.

A continuous, gradational surface was created for the Al-OH and Fe-OH wavelength positions in order to visualize the spatial trends of the ground spectra. This was accomplished by using the nearest ten wavelength positions within a 200 m radius to calculate the contents of each pixel in the surface via the IDW (Inverse Distance Weighting) interpolation tools of the ArcGIS software package (Cressman, 1959; Shepard, 1968; Philip and Watson, 1982; ESRI, 2011). The diameter of the interpolated surface around each ground spectral observations (200 m) was chosen based on the spatial distribution of the Al-OH and Fe-OH wavelength position observations. More

specifically, this diameter was estimated using the average and maximum distances of each Al-OH (average: 87 m, maximum: 383 m) and Fe-OH (average: 105 m, maximum: 1333 m) absorption feature field measurement to the nearest field measurement. The 200 m radius was estimated based on these average and maximum distances to minimize extrapolation and to create a realistic representation of the spatial trends of the absorption feature wavelength positions in the study area. The resulting surface was normalized and divided into four quartiles to highlight the spatial distribution of the shortest and longest quartile (25%) of the Al-OH and Fe-OH wavelength positions.

In a separate analysis, the Al-OH and Fe-OH wavelength positions were examined in the context of the location of the rhyolitic rock outcrops relative to the nearest massive sulfide lens. This was carried out to reveal the possible spatial trends of the wavelength positions within the study area with respect to the ore zones. Only the intensely altered areas (as defined by the $Na_2O$ isopleth maps of Morrison (2004); see Fig. 1) were included in this analysis and hence areas distal to the massive sulfide lenses (within 5800-6800 m) were omitted.

*5.2 Airborne spectrometric data processing*

Airborne data collected over the study area were used to map the spatial distribution of the Al-OH wavelength positions of the rhyolitic rocks in the study area. The spatial distribution of the Fe-OH absorption feature wavelengths was investigated, but these absorption features were left out of the analysis because this specific absorption feature was not readily identified in the airborne spectrometry. More specifically, the Fe-OH absorption features were estimated to be too weak to be reliably detectable by remote sensing means. As a first pre-processing step, the full airborne dataset was clipped to correspond to the estimated dimensions (1.9 $km^2$) of the rhyolitic rock outcrops in the study area map provided by MMG. Next, the image was processed

in three steps: i) pixels attributed to vegetation were removed, ii) spectral unmixing was performed to remove pixels most impacted by the effects of lichens, and iii) the wavelength position of the Al-OH absorption absorption feature in all remaining pixels was determined.

The chlorophyll index developed by Gitelson and Merzlyak (1994, Normalized Difference Vegetation Index $NDVI_{705}$) was used to identify pixels attributed to photosynthetic vegetation. This index uses wavelengths 705 nm and 750 nm in the visible and near-infrared wavelength regions, along the "red edge" spectral feature of vegetation to detect attributes such as the chlorophyll content (Sims and Gamon, 2002). Next, a threshold value of 0.2 was applied to the $NDVI_{705}$ results to mask out pixels associated with vegetation. This threshold was chosen based on the results of Gitelson and Merzlyak (1994), who attributed $NDVI_{705}$ values greater than 0.2 with increasing chlorophyll content of vegetation. The masked pixels comprise 80% of the total number of pixels covering rhyolitic rock outcrops ($n$=75499).

Spectral endmembers were extracted from the remaining airborne pixels by means of the spatial-spectral endmember extraction (SSEE) tool of Rogge et al. (2007). SSEE comprises three steps where the image is first divided into equal sized non-overlapping subset regions where a set of eigenvectors that explain most of the spectral variance is calculated for each subset. Then the image data are projected onto the local eigenvectors compiled from all subset regions and the pixels occupying either extreme of the vectors are retained as candidate endmembers. Lastly, within a given spatial window, the candidate pixels are averaged with all other pixels that are spectrally similar. One hundred and thirty seven endmembers were obtained through this endmember extraction process, of which 22 were chosen to represent rocks, vegetation and lichens, or any mixtures thereof. This endmember spectral database of 22 endmembers served as input for the linear spectral unmixing computer calculations

(Adams et al., 1993; Boardman, 1993; Settle and Drake, 1993). The resulting 22 abundance fraction images were analyzed and attributed to lichen, vegetation, or lichen-rock or vegetation-rock mixtures, based on their spectral characteristics. A single lichen-coated endmember image was chosen to represent pixels of rhyolitic rock outcrops that have a minimal lichen cover, and a threshold of 0.6 (fractional abundances of 60 % or higher) was applied to this endmember image to retain rhyolitic rock outcrop pixels with sparse vegetation and lowest degree of lichen cover. After this procedure, 1% of the original number of pixels associated with the rhyolitic rock outcrops remained in the dataset.

Next, the wavelength position of the Al-OH absorption feature was calculated after hull removal from the 2188-2212 nm wavelength range. This absorption feature wavelength position range was chosen because it encompasses the wavelength range of absorption features present in the ground spectra (see below). Upon analysis of the airborne spectra, the 2212 nm wavelength position was masked out because it was deemed to be associated with lichens and other vegetation rather than rock outcrops. Similarly, the 2194 nm Al-OH wavelength in the airborne spectrometry was left out of further analysis because the spectral shape of the absorption features in this wavelength range are strongly influenced by lichens and do not represent rhyolitic rock outcrops. The basis for masking out these absorption features is the near absence of an absorption feature at 2194 nm and 2212 nm in ground spectra, whereas these absorption features are ubiquitously present in the airborne spectrometry, suggesting association with other elements than rhyolitic rocks. It is also notable that the necessity to further mask out pixels suggests that the abundant lichen cover on the rock outcrops of the study area prevented a complete separation of lichens and rock surfaces through spectral unmixing. One factor that may have contributed to this result is the spectral variation of vegetation with varying nitrogen, cellulose and lignin contents. The spectral shape of plants varies

as a function of these chemical elements and compounds (Kokaly et al., 2009), which can increase the spectral diversity and make endmember extraction more challenging.

At this stage, 261 pixels remained, representing 0.3% of the original amount of pixels associated with the rhyolitic rock outcrops. The inverse distance weighting (IDW) interpolation tools (Cressman, 1959; Shepard, 1968; Philip and Watson, 1982) were then used to create a continuous surface of the Al-OH absorption feature wavelength positions of these pixels by employing the nearest 15 Al-OH absorption feature wavelengths to calculate the contents of each pixel in the interpolated surface. The interpolated surface was cropped to a 200 m buffer around each observation in order to minimize the effects of extrapolation to areas of no observations.

The results were then validated against ground spectrometry. The averaged spectra of each rock outcrop measured in the field was then re-sampled to the sampling interval of the ground spectrometry (1 nm in the SWIR wavelength region) to the sampling interval of the airborne spectrometry (6.3 nm). Each Al-OH absorption feature wavelength position ($n$=261) in the airborne spectrometric dataset was then linked with its geographically nearest Al-OH absorption feature wavelength position ($n$=98), extracted from the ground spectrometry. These observations were then compared, and the accuracy of the airborne Al-OH absorption feature wavelength position was assessed based on how well each observation corresponded to the spatially nearest ground spectral observation. More specifically, the accuracy was assessed based on the difference (in nm) between the Al-OH absorption feature wavelength positions of the airborne and ground spectral datasets.

## 6. Results

### *6.1 Mineralogy*

All samples examined under the microscope (51, 53, 54, 55, 56 and 59) are fine-

grained (average 0.2 mm), and some display mineralogical banding. White micas are present in four samples, biotite in five samples and chlorite in one sample (Figs. 3A-F, Table 1). White micas are responsible for the Al-OH absorption features, and biotite or chlorite are associated with the Fe-OH absorption features of the samples. However, this match is not perfect, as sample 53 does not reveal white micas in the thin section investigated despite the presence of an Al-OH absorption feature. In all likelihood the spatial distribution of white micas is inhomogeneous in sample 53.

*6.2 Mineral chemistry*

Table 2 summarizes the mineral compositions for white micas, chlorite, and biotite, as determined by EMPA for the seven samples (PTS) and the average Al-OH and Fe-OH wavelength positions obtained from the corresponding hand specimen. Analysis of the EMPA data revealed a strong correlation between the Fe-OH wavelength position and the Mg/(Mg+Fe) ratio of biotite/chlorite (Pearson's $r$=-0.893, $n$=7, $p$=0.007, 99% confidence level, two-tailed) (Fig. 4A). Similarly, correlation analysis shows a strong, statistically significant correlation between the Al-OH wavelength positions and the Si/Al ratio of white micas (Pearson's $r$=0.861, $n$=6, $p$=0.028, 95% confidence level, two-tailed, Fig. 4B). Furthermore, a strong correlation (Pearson's $r$=0.849, $n$=6, $p$=0.032, 95% confidence level, two-tailed) exists between the Al-OH wavelength position and the Mg+Fe content of white micas (Fig. 4C). Ratios that measure the amount of Na (sodic content) in the mineral lattice of white micas are not applied in this analysis, because the shortest wavelength position of the white micas is at relatively long wavelengths (2198 nm), indicating that none of the samples are truly sodic (i.e. paragonitic).

These relationships between the average Al-OH and Fe-OH wavelength positions, and the chemical composition of the samples indicate that the absorption

feature wavelength positions vary systematically with the chemical composition of muscovite and biotite/chlorite. More specifically, the Al-OH wavelength position of the white micas decreases with increasing Al content (measured by the Si/Al ratio) and increases with increasing Mg+Fe content. Similarly, the Fe-OH wavelength position of biotite/chlorite decreases with increasing Mg/(Mg+Fe) ratio (increasing Mg content).

### *6.3 Ground spectrometry*

#### *6.3.1 Frequency and spatial distribution of the Fe-OH absorption feature wavelength positions*

The Fe-OH absorption is present in spectra from 85 of the rhyolitic rock outcrops, (79%, $n$=108). The frequency distribution of these wavelength positions is shown in Figure 5A, and ranges from 2249 nm to 2259 nm (mean=2254 nm, mode=2255 nm, std. dev.=2.078). This broad wavelength range and the presence of values on the extremes of the wavelength positions are illustrated in Figures 5B,C. The Shapiro-Wilk normality test shows that the wavelength positions are normally distributed ($p$=0.703) and there are no outliers in the dataset.

The broad wavelength range of the Fe-OH absorption feature wavelengths is also evident in their spatial distribution, shown in Figure 6A. Furthermore, the Fe-OH absorption feature wavelengths form two distinct spatial groups that are apparent upon comparison of the average Fe-OH wavelength position of the proximal (398-3146 m from the massive sulfides) and distal (5782-6812 m from the massive sulfides) areas. The proximal area (”area 1” in Fig. 6A) of 73 measured rock outcrops has an average Fe-OH absorption feature wavelength position at 2254 nm (std. dev.=1.831), whereas the distal area (”area 2” in Fig. 6A) comprised of 12 rhyolitic rock outcrops, has an average Fe-OH wavelength position at 2251 nm (std. dev.=1.215). This trend toward shorter Fe-OH absorption feature wavelength positions is also apparent in the bivariate

plot of the Fe-OH absorption feature wavelength positions versus distance from 3146 m to the nearest massive sulfide lens (Fig. 6B). Furthermore, there is a statistically significant inverse correlation between the Fe-OH wavelength position and the distance to the massive sulfide lenses (Pearson's $r$=-0.324, $p$=0.0, $n$=73), at the 99% confidence level.

*6.3.2 Frequency and spatial distribution of the Al-OH absorption feature wavelength positions*

An Al-OH absorption feature is present in 98 (91%) spectra from rhyolitic rock outcrops, indicating that the minerals responsible for this spectral feature are abundant throughout the study area. The average wavelengths of the absorption features in these outcrops varies between 2194 nm and 2211 nm (mean=2203 nm, mode=2202 nm, std. dev.=3.084; Fig. 7A). The wide range of the absorption feature wavelengths results from spectral shifts, illustrated in Figures 7B,C. According to the Shapiro-Wilk normality test, the frequency distribution of the absorption feature wavelength positions is normally distributed ($p$=0.063, $n$=98); furthermore, according to an outlier test, the wavelength positions less than or equal to 2195 nm and greater than or equal to 2210.5 nm are outliers. However, after careful analysis of the associated spectra, these wavelength positions were deemed not to be outliers, and for this reason were not removed from the dataset. The extreme Al-OH wavelength positions likely indicate the presence of sodic and phengitic muscovite that have characteristic spectral shifts toward shorter and longer wavelengths, respectively (Duke, 1994).

There is no statistically significant Pearson correlation between the averaged Al-OH absorption feature wavelengths of the rhyolitic rock outcrops and the distance to the nearest massive sulfide. However, there is a slight shift toward longer wavelengths in the proximal areas (327-2679 m from the massive sulfides) as opposed to the distal areas

(5782-6812 m from the massive sulfides). In the proximal areas (”area 1” in Fig. 8A) the average Al-OH absorption feature wavelength of the rhyolitic rock outcrops is 2203 nm (*n*=85, std. dev.=2.983), whereas in the distal areas (”area 2” in Fig. 8A) the corresponding average wavelength position is 2201 nm (*n*=13, std. dev.=3.165), but this is a displacement essentially of only one band. Visual inspection of the results (Fig. 8A), shows that the massive sulfide lenses are surrounded by relatively high Al-OH absorption feature wavelengths, so that the highest values are located northwest of the massive sulfide lenses. This is also evidenced by a cluster of the upper quartile (highest 25%) Al-OH absorption feature wavelength positions in the vicinity of Izok Lake (Fig. 8B). Despite this apparent trend in the Al-OH absorption feature wavelength positions in the study area, relatively long wavelength positions occur both in the proximal and distal areas, indicating that the Al-OH absorption feature wavelength positions do not vary systematically with distance from the massive sulfide lenses.

### *6.4 Airborne spectrometry*

#### *6.4.1 Frequency and spatial distribution of the Al-OH absorption feature wavelength positions*

The frequency distribution of the Al-OH absorption feature wavelength positions of the airborne data (*n*=261) define two groups: one at 2200 nm and the other at 2206 nm (Fig. 9A). The mode and median of the airborne data are both at 2200 nm, and these coincide with the mode and median of the ground spectrometry, that has been re-sampled to the sampling interval of the airborne spectrometry (Fig. 9B). Although the values for both the airborne spectrometry and the re-sampled ground spectrometry are identical, the Al-OH wavelength range of the former is relatively narrow compared to that of the latter (2194-2212 nm, Figs. 9A,B), indicating that the entire wavelength position range of the Al-OH absorption feature is not detected in the airborne

spectrometric dataset. This conclusion is also suggested by the relatively low accuracy of the airborne spectrometry as measured by the difference between the ground and airborne spectra. Sixty five percent of the Al-OH absorption feature wavelength positions in the airborne data ($n$=169) are within three nanometers of their spatially nearest airborne spectrometric value. Within this 65% of observations, there is a strong, statistically significant positive Pearson correlation ($r$=0.917, $p$=0.0, $n$=169, 99% confidence level, one-tailed), between the ground and airborne spectra.

The average airborne Al-OH absorption feature wavelength positions in the proximal (”area 1” in Fig. 10A, $n$=182) and distal (”area 2” in Fig. 10A, $n$=9) areas, are both 2201 nm, indicating that there is no systematic trend in the airborne Al-OH wavelength positions with distance to the massive sulfide lenses. Despite this, there is a zone of relatively long Al-OH absorption feature wavelength positions in the airborne spectrometry in the vicinity of the massive sulfide lenses. This area, located 800-1900 m west of the sulfide lenses, and shown as an "area of enhanced alteration" in Figures 10A,B, coincides spatially with several $4^{th}$ quartile (the highest 25% of the ground observations at wavelengths between 2207-2211 nm) areas in the ground spectrometry, shown in Figure 10B. There are also indications of a spatial continuity of long Al-OH absorption feature wavelengths 1500 m north and 1000 m south of the massive sulfide lenses. Based on the Al-OH absorption features extracted from the airborne spectrometry alone, the areal extent of this alteration zone is ≈8.67 $km^2$.

## 7. Discussion

### *7.1 Validation of the ground spectroscopic datasets*

The mineralogical composition of the samples was determined by optical microscopic study of PTS. The presence or absence of the Al-OH and Fe-OH absorption features was compared to the petrographic data for the corresponding PTS. The results

indicate that the Al-OH absorption feature is associated with white micas and the Fe-OH absorption feature is associated with biotite and chlorite. However, there is incomplete correspondence between the presence of Al-OH absorption features and the presence of white micas, as an Al-OH absorption feature was detected in sample 53, despite the absence of muscovite in the PTS for this sample (Table 1). This is likely due to the inhomogeneous distribution of white mica in sample 53. The discrepancy between the sizes of the thin sections (26 X 46 mm) and the areas used for making spectral measurements from the samples (on average 100 $cm^2$) entails that there will only be a perfect correlation between the two in samples with homogenously distributed minerals.

The spectral results were further validated by comparing the spectral shifts of the Al-OH and Fe-OH absorption features to the chemical compositions of biotite, chlorite and white micas in the corresponding samples. The results, shown in Figure 4 and listed in Table 2, indicate that there is a strong positive correlation between the Si/Al content of white micas and the average Al-OH absorption feature wavelength position. Furthermore, there is a correlation of similar magnitude and direction between the average Al-OH wavelength position of a sample and the Mg+Fe content of its white micas. In contrast, a strong inverse correlation exists between the average Fe-OH wavelength position and the Mg/(Mg+Fe) content of biotite/chlorite within the same sample. These results indicate that the increasing Al content of white micas and the increasing Mg content of biotite/chlorite are associated with the shifts toward shorter wavelengths of the Al-OH and Fe-OH absorption features, respectively. The inverse is true for the increasing Mg,Fe content of the white micas, and Fe content of biotite and chlorite, which is associated with the shifting toward longer wavelengths of the Al-OH and Fe-OH absorption feature wavelength positions. Our findings are consistent with the results of previous studies of Bassett (1960), McLeod et al. (1987), Post and Noble (1993) and Duke (1994) who have documented similar spectral shifts in association with

the chemical compositional variation of biotite, chlorite and muscovite.

*7.2 Absorption feature wavelength positions of white micas and chlorite group minerals*

There is considerable variation in the Al-OH and Fe-OH absorption feature wavelength positions of white mica and biotite/chlorite in the Izok Lake area. These variations likely result from hydrothermal alteration processes active at the time of the massive sulfide formation. The Al-OH wavelength range demonstrated by the ground spectrometry (2194-2211 nm) indicates that the chemical composition of white micas ranges from paragonitic (short wavelength positions near 2195 nm) to muscovitic (wavelength positions near 2200 nm) to slightly phengitic (wavelength position near 2210 nm). Similarly, the chemical compositions of chlorite group minerals range from Mg-rich to Mg-Fe-rich, based on the Fe-OH wavelength positions extracted from the ground dataset. This Mg-rich and Mg-Fe rich chlorite classification is in accordance with the results by Yang and Huntington (1996), who documented Mg-rich chlorite associated with the Fe-OH absorption features between 2252 and 2254 nm, and Mg-Fe chlorite associated with the Fe-OH absorption feature wavelengths between 2256 and 2262 nm. The observed Al-OH and Fe-OH absorption feature wavelength distributions also suggest that the chemical compositional changes within biotite, chlorite and muscovite result in broad and continuous wavelength position data distributions that should be analyzed by means of high spectral resolution datasets with narrow bandpass sampling intervals.

*7.3 Absorption feature wavelength trends in the ground spectra*

The spectral shifts of the Fe-OH absorption features in the ground data were studied by plotting the absorption feature wavelength positions against their distances to the known massive sulfide lenses (Fig. 6B). This bivariate plot, and an interpolated

surface (Fig. 6A), created from the Fe-OH absorption feature wavelength positions, reveal systematic trends in the Fe-OH absorption feature wavelength positions with distance to the known massive sulfide lenses. This trend is manifested as a shift toward longer Fe-OH absorption feature wavelengths in the area proximal to the massive sulfide lenses (within 300-3100 m), and a shift toward shorter wavelengths in the areas distal from the massive sulfide lenses (within 5800-6800 m). The implication is that altered rocks proximal to the Izok Lake massive sulfide lenses contain Mg-Fe biotite/chlorite, and the distal areas contain Mg-rich biotite/chlorite. Contrary to the observed spatial variability of the Fe-OH absorption feature wavelength, no spatial variability of the Al-OH absorption feature wavelength with respect to distance from massive sulfide lenses was discerned. However, an area of relatively long Al-OH wavelength positions, revealed by an interpolated surface, occurs in the vicinity of the massive sulfide lenses, coinciding with the area of Mg-Fe biotite/chlorite. The long Al-OH wavelength positions of this area (up to 2211 nm) indicate the presence of slightly phengitic muscovite.

*7.4 Absorption feature wavelength trends in the airborne spectrometry*

In order to place the spectral shifts of the Al-OH wavelength positions in the ground spectrometry into a regional context, these data were scaled up to the airborne spectrometry. A comparison between the airborne and ground spectra reveals a detection accuracy of 65%, when each accurately detected airborne Al-OH absorption feature wavelength position was determined to lie within three nanometers from the Al-OH absorption feature wavelength position of the spatially nearest ground spectrum. Problems in the detection of the spectral properties of rock outcrops in the study area, indicated by this relatively low accuracy of the airborne spectrometry, may result from multiple factors, including the abundant vegetation and lichen cover that necessitated the

masking out of 99% of the pixels associated with the rhyolitic rock outcrops in the airborne dataset.

One factor that affects the ability to detect the spectral features of rocks is the sampling interval of the dataset. This is demonstrated in Figure 11 that shows the Al-OH absorption feature wavelength positions of the ground spectra (sampling interval: 1 nm; Figs. 11A,B) and ground spectra resampled to the sampling interval of the airborne spectra (sampling interval: 6.3 nm; Figs. 11C,D). As the sampling interval is decreased from 1 nm to 6.3 nm, the Al-OH absorption feature wavelength positions shift from 2202 nm to 2200 nm (spectrum 2, Figs. 11B,D) and from 2208 nm to 2206 nm (spectrum 1, Figs. 11B,D). Moreover, as expected the signal-to-noise ratio of the airborne spectral dataset is lower than that of the ground spectral dataset. This is evident in Figures 11E,F that show four representative single pixel spectra extracted from the rhyolitic rock outcrops of the airborne spectral dataset. Spectra 2 and 4 have an absorption near 2206 nm and 2200 nm, respectively, whereas spectra 1 and 3 have an absorption near 2194 nm and 2212 nm, respectively. Spectra with an absorption feature near 2200 nm and 2206 nm, extracted from the rhyolitic rock outcrops of the study area, were interpreted to be associated with white micas. When comparing spectra 2 and 4 with spectra 1 and 3 it becomes evident that the absorption of spectra 2 and 4 is slightly broader. However, the overall spectral shape of all the spectra in Figure 11E is similar and all have an absorption feature near 2100 nm, indicating spectral mixing between rocks and lichens. Thus the main reason for masking out the absorption features shorter than 2200 nm and longer than 2206 nm was the discrepancy between the data distributions of the Al-OH absorption feature wavelength positions of the ground spectra and that in the airborne data when the full spectral range of the Al-OH absorption features of the ground spectra (2194-2211 nm, Fig. 7A) were taken into account.

The problems in detecting the spectral properties of the rock outcrops may be

exacerbated by the relatively small proportion of sodic and phengitic micas in the study area, as determined by the distribution of the Al-OH absorption feature wavelengths in the ground spectrometry (Fig. 7A). Lesser abundances of minerals result in shallower absorption feature depths (Clark, 1999), and for this reason detecting minerals present in lower abundances (e.g. phengitic muscovite in the Izok Lake area) is more challenging than detection of more abundant minerals that have clearly expressed absorption features.

The abundance of biotite and chlorite may also play a role in the detection of their absorption features in the airborne spectrometry. An Fe-OH absorption feature associated with these minerals is present in only 79% of the ground spectra, whereas an Al-OH absorption feature attributed to white micas occurs in 91% of the ground spectra. The higher detection percentage of the Al-OH absorption feature suggests that white micas are more uniformly distributed in the study area than biotite/chlorite. Moreover, the average Fe-OH absorption feature band depth of the ground spectra is 3.3%, whereas the average Al-OH absorption feature band depth of the ground spectra is 20% (scale: 0-100%). The depth of an absorption is related to the abundance of the absorber (Clark, 1999) and hence the discrepancy between the Al-OH and Fe-OH absorption band depths indicates that the minerals inducing the former absorption feature are more abundant than the minerals inducing the latter absorption feature. This more uneven distribution and lesser abundance of biotite/chlorite (as opposed to white micas) is the likely determining factor for the lack of detection of biotite/chlorite in the airborne spectra. Other factors, such as the quality of preprocessing (e.g. atmospheric correction), S/N (signal-to-noise) ratio, sampling interval and band pass of the spectral data can also influence the ability to detect spectral features (Swayze et al., 2003).

Although the detection accuracy of the airborne spectrometry is relatively low, the ability to detect an area of phengitic muscovite using both the ground and airborne datasets independently demonstrates the efficacy of airborne spectrometry for the

recognition and delineation of zones of hydrothermally altered rocks in outcrops in the Izok Lake area.

*7.5 Implications for the interpretation of the deposit fluid flow paths*

An area of altered rocks with relatively long Al-OH absorption feature wavelengths of the ground and airborne spectra (Figs. 10A,B) was identified in the vicinity of the massive sulfide lenses of the Izok Lake deposit. This area contains phengitic muscovite and intermediate to Fe-rich chlorite, both of which formed at high temperature (200-350°C; Hulen and Nielson, 1986; Cathelineau, 1988). In addition to temperature, another influence on the chemical composition of white micas and chlorite group minerals is the chemical composition of the hydrothermal fluids (Cathelineau, 1988). Elevated $Mg^{2+}$ and $Fe^{2+}$ (relative to $Al^{3+}$) contents of the hydrothermal fluid favor the formation of phengite (Yang et al., 2011). Thus, the area of altered rocks with long Al-OH absorption feature wavelengths may reflect interaction with high-temperature, metal-rich, and moderately acidic hydrothermal fluids (Lentz and Goodfellow, 1993), possibly within or at the margin of a fluid discharge zone.

The chemical composition of chlorite is controlled largely by bulk rock compositions (Inui and Toriumi, 2004), and a shift toward more Fe-rich biotite/chlorite in this area corroborates this interpretation, as a characteristic feature of focused fluid discharge sites is their Fe-rich bulk compositions (e.g., Barrett and MacLean, 1994). The area of long Al-OH absorption feature wavelengths partly coincides with an area of the intense hanging wall alteration discussed by Morrison (2004) that he interpreted to be an area of sub-seafloor replacement.

## 8. Summary and Conclusions

Our ground hyperspectral results indicate that there is a systematic trend in the

Fe-OH absorption feature wavelength position of biotite/chlorite with distance from the VMS deposit. No such trend was identified in the Al-OH feature of white micas, but a spatial pattern of relatively long Al-OH absorption feature wavelength positions was observed in the vicinity of Izok Lake using ground and airborne hyperspectral sensors. This area coincides with relatively long Fe-OH absorption feature positions, detected by means of a ground hyperspectral sensor. These findings indicate that hydrothermal alteration zones can be detected by hyperspectral remote sensing, despite the presence of abundant lichen cover in the study area.

The large ranges in the Al-OH and Fe-OH absorption feature wavelengths of muscovite and biotite/chlorite in the Izok Lake area reflect large chemical compositional variations in these minerals. Unlike the white micas that display more spatial variation in their Al-OH wavelength positions, the Fe-OH wavelength positions of biotite/chlorite display consistent and systematic spatial shifts toward longer wavelengths in areas proximal to the massive sulfide mineralization and a shift toward shorter wavelengths in areas distal to the massive sulfides. These shifts indicate that biotite/chlorite becomes more Fe-rich in the vicinity of the ore deposit and more Mg-rich in the distal areas.

Unfortunately, the Fe-OH absorption feature associated with biotite/chlorite could not be detected in the airborne spectrometry, and hence the large-scale trends of the chemical composition of these phyllosilicate minerals remain unconstrained. However, an alteration halo comprising phengitic white micas was detected and delineated using both the ground and airborne spectral datasets. Based on ground spectrometry, this phengitic alteration halo coincides with a zone of Mg-Fe biotite/chlorite proximal to the massive sulfide lenses. This fluid upflow alteration zone extends ≈1000 m south, 1500 m north and 1900 m west of the Izok Lake deposit. Despite the low detection accuracy of the airborne data, the ability to identify this hydrothermal alteration zone using airborne hyperspectral remote sensing data shows

that this method has great promise in identifying and delineating zones of chlorite and white mica hydrothermally altered rock that may be associated with VMS and other hydrothermal mineral deposits (e.g., orogenic gold) in regions that have considerable lichen cover. This lends support for the development of future airborne and spaceborne hyperspectral sensors of higher signal-to-noise ratios and spectral resolutions that would allow for better spectral unmixing and separation of cellulose and non-photosynthetic vegetation materials from white mica minerals indicative of VMS environments.

Our study also highlights the importance of careful selection of wavelengths for image analysis in environments where the spectral signatures are strongly influenced by spectral mixing. Two absorption feature wavelength positions (2194 nm and 2212 nm) were discarded from the airborne dataset due to the effects of spectral mixing of rocks and vegetation that could not be completely eliminated through spectral unmixing and band ratio analysis of vegetation (NDVI). This step proved essential for obtaining relatively accurate results from the airborne data, regardless of the loss of significant portions of the data.

## Acknowledgments

Funding for 2011-2014 came from the Research Affiliate and the Targeted Geoscience Initiative 4 (TGI-4) Programs of the Earth Sciences Sector, Natural Resources Canada. The hyperspectral airborne data were acquired under the Strategic Investment in Northern Economic Development (SINED) Program of Indian and Northern Affairs Canada (now Aboriginal and Northern Affairs Canada), and we gratefully acknowledge the contributions of Donald James in facilitating the survey. We thank Minerals and Metals Group Ltd., particularly Kimberley Bailey, Trish Toole, Ian Neill, and Dave Kelley, for logistical and field support in 2010 and 2013 in for geological discussions and access to company data. The Department of Geosciences and

Geography of the University of Helsinki are thanked for use of their petrographic sample preparation facilities. Our sincerest thanks also go to Katherine Venance (Geological Survey of Canada) for conducting the electron microprobe analyses. This is GSC Contribution # 20140146. Finally, we would like to thank Dr. Bernard Hubbard, Dr. Ray Kokaly and Dr. Jeanne Percival for their many suggestions for improving this paper.

## References

Adams, J. B., Smith, M. O. and Gillespie, A. R., 1993, Imaging spectroscopy: Interpretation based on spectral mixture analysis, in Pieters, C.M. and Englert, P.A., eds., Remote geochemical analysis: Elemental and mineralogical composition: Cambridge University Press, Cambridge, UK, p. 145−166.

Ager, C. M. and Milton, N. M., 1987, Spectral reflectance of lichens and their effects on the reflectance of rock substrates: Geophysics, v. 52, p. 898–906.

Barrett, T.J. and MacLean, W.H., 1994, Mass changes in hydrothermal alteration zones associated with VMS deposits of the Noranda area: Exploration and Mining Geology, v. 3, p. 131–160.

Bassett, W.A., 1960, Role of hydroxyl orientation in mica alteration: Bulletin of the Geological Society of America, v. 71, p. 449–456.

Bechtel, R., Rivard, B., and Sánchez-Azofeifa, A., 2002, Spectral properties of foliose and crustose lichens based on laboratory experiments: Remote Sensing of Environment, v. 82, p. 389-396.

Boardman, J.W., 1993, Automating spectral unmixing of AVIRIS data using convex geometry concepts: Summaries of the fourth annual JPL (Jet Propulsion Laboratory) airborne geoscience workshop, JPL publication 93-26, AVIRIS Workshop, v. 1, Washington, USA, p. 11–14.

Bostock, H.H., 1980, Geology of the Itchen Lake area, district of Mackenzie: Geological Survey of Canada, Memoir 391, Canadian Government Publishing Centre, Québec, 101 p.

Bruegge, C.J., Stiegman, A.E., Rainen, R.A. and Springsteen, A.W., 1993, Use of Spectralon as a diffuse reflectance standard for in-flight calibration of earth-orbiting sensors: Optical Engineering, v. 32, p. 805-814.

Cathelineau, M., 1988, Cation site occupancy in chlorites and illites as a function of temperature: Clay Minerals, v. 23, p. 471–485.

Clark, R.N., 1999, Chapter 1: Spectroscopy of rocks and minerals, and principles of spectroscopy, in Rencz, A.N., ed., Manual of Remote Sensing, v. 3: New York, Wiley, p. 3–58.

Clark, R.N. and Roush, T.L., 1984, Reflectance spectroscopy: quantitative analysis techniques for remote sensing applications: Journal of Geophysical Research, v. 89, p. 6329–6340.

Clark, R.N., Swayze, G.A., Livo, K.E., Kokaly, R.F., King, T.V.V., Dalton, J.B., Vance, J.S., Rockwell, B.W., Hoefen, T. and McDougal, R.R., 2002, Surface reflectance calibration of terrestrial imaging spectroscopy data: A tutorial using AVIRIS: Proceedings of the 10th Airborne Earth Science Workshop, JPL Publication 02-1.

Clark, R.N., Swayze, G.A., Wise, R., Livo, E., Hoefen, T., Kokaly, R. and Sutley, S.J., 2007, USGS digital spectral library splib06a: U.S. Geological Survey, Digital Data Series 231 (http://speclab.cr.usgs.gov/spectral.lib06).

Cressman, G.P., 1959, An operational objective analysis system. Monthly Weather Review: v. 87, p. 367-374.

Duke, E.F., 1994, Near infrared spectra of muscovite, Tschermak substitution, and metamorphic reaction progress: Implications for remote sensing: Geology, v. 22, p. 621–624.

Eberl, D.D., Środoń, J., Lee, M., Nadeau, P.H. and Northrop, H.R., 1987, Sericite from the Silverton caldera, Colorado: Correlation among structure, composition, origin, and particle thickness: American Mineralogist, v. 72, p. 914-934.

ESRI, 2011, ArcGIS Desktop: Release 10. Redlands, CA: Environmental Systems Research Institute.

Galley, A., Hannington, M. and Jonasson, I., 2007, Volcanogenic Massive Sulphide Deposits, in Goodfellow, W.D., ed., Mineral Deposits of Canada. A synthesis of major deposit-types, district metallogeny, the evolution of geological provinces, and exploration methods: Geological Association of Canada, Mineral Deposits Division, Special publication, v. 5, p. 141–161.

Gitelson, A. and Merzlyak, M.N., 1994, Spectral reflectance changes associated with autumn senescence of *Aesculus hippocastanum* L. and *Acer platanoides* L. leaves. Spectral features and relation to chlorophyll estimation: Journal of Plant Physiology, v. 143, p. 286–292.

Government of Canada, 2014, Calculation of the 1971 to 2000 climate normals for Canada (http://climate.weather.gc.ca/climate_normals/).

Guidotti, C.V. and Sassi, F.P., 1998, Petrogenetic significance of Na-K white mica mineralogy: Recent advances for metamorphic rocks: European Journal of Mineralogy, v. 10, p. 815–854.

Herrmann, W., Green, G., Barton, M. and Davidson, G., 2009, Lithogeochemical and stable isotopic insights into submarine genesis of pyrophyllite-altered facies at the Boco Prospect, Western Tasmania: Economic Geology, v. 104, p. 775–792.

Hitchcock, R. and White, H.P., 2007, Processing EO-1 Hyperion data using ISDAS, Geomatics, Canada, Technical Note 2, 30 p.

Hulen, J.B. and Nielson, D.L., 1986, Hydrothermal alteration in the Baca geothermal system, Redondo Dome, Valles Caldera, New Mexico: Journal of

Geophysical Research, v. 91, p. 1867– 1886.

Inui, M. and Toriumi, M., 2004, A theoretical study on the formation of growth zoning in garnet consuming chlorite: Journal of Petrology, v. 45, p. 1369–1392.

Jones, S., Herrmann, W. and Gemmell, J.B., 2005, Short wavelength infrared spectral characteristics of the HW horizon: Implications for exploration in the Myra Falls Volcanic-Hosted Massive Sulfide Camp, Vancouver Island, British Columbia, Canada: Economic Geology, v. 100, p. 273–294.

Kokaly, R.F., Asner, G.P., Ollinger, S.V., Martin, M.E. and Wessman, C.A., 2009, Characterizing canopy biochemistry from imaging spectroscopy and its application to ecosystem studies: Remote Sensing of Environment, v. 113, p. S78-S91.

Kranidiotis, P. and MacLean, W., 1987, Systematics of chlorite alteration at the Phelps Dodge massive sulfide deposit, Matagami, Quebec: Economic Geology, v. 82, p. 1898–1911.

Laidler, G.J., Treitz, P.M. and Atkinson, D.M., 2008, Remote sensing of Arctic vegetation: Relations between the NDVI, spatial resolution and vegetation cover on Boothia Peninsula, Nunavut: Arctic, v. 61, p. 1–13.

Lentz, D.R. and Goodfellow, W.D., 1993, Petrology and mass-balance constraints on the origin of quartz-augen schist associated with the Brunswick massive sulfide deposits, Bathurst, New Brunswick: The Canadian Mineralogist, v. 31, p. 877-903.

Li, G., Peacor, D.R., Merriman, R.J. and Roberts, B., 1994, The diagenetic to low-grade metamorphic evolution of matrix white micas in the system muscovite-paragonite in a mudrock from Central Wales: Clays and Clay Minerals, v. 42, p. 369-381.

Longton, R.E., 1988, Biology of polar bryophytes and lichens: Cambridge University Press, Cambridge, 391 p.

McLeod, R.L., Gabell, A.R., Green, A.A. and Gardavsky, V., 1987, Chlorite infrared spectral data as proximity indicators of volcanogenic massive sulphide mineralization: Pacific Rim Congress (The Geology, Structure, Mineralisation and Economy of the Pacific Rim), Gold Coast, Australia, p. 321–324.

Miyashiro, A. and Shido, F., 1985, Tschermak substitution in low- and middle-grade pelitic schists: Journal of Petrology, v. 26, p. 449–487.

Morrison, I.R., 2004, Geology of the Izok massive sulfide deposit, Nunavut Territory, Canada: Exploration and Mining Geology, v. 13, p. 25–36.

Mortensen, J.K., Thorpe, R.I., Padgham, W.A., King, J.E. and Davis, W.J., 1988, U-Pb zircon ages for felsic volcanism in Slave Province, N.W.T., in Radiogenic Age and Isotopic Studies, report 2: Geological Survey of Canada, Paper 88-2, p. 85–95.

Philip, G.M. and Watson, D.F., 1982, A precise method for determining contoured surfaces: Australian Petroleum Exploration Association Journal, v. 22, p. 205-212.

Post, J.L. and Noble, P.N., 1993, The near-infrared combination band frequencies of dioctahedral smectites, micas, and illites: Clays and Clay Minerals, v. 41, p. 639–644.

Purvis, W., 2000. Lichens, Smithsonian Institution Press, Washington, USA, 112 p.

Richter, R. and Schläpfer, D., 2002, Geo-atmospheric processing of airborne imaging spectrometry data. Part 2: Atmospheric/topographic correction: International Journal of Remote Sensing, v. 23, p. 2631-2649.

Rivard, B. and Arvidson, R.E., 1992, Utility of imaging spectrometry for lithologic mapping in Greenland: Photogrammetric Engineering & Remote Sensing, v. 58, p. 945–949.

Rogge, D.M., Rivard, B., Zhang, J., Sanchez, A., Harris, J. and Feng, J., 2007,

Integration of spatial-spectral information for the improved extraction of endmembers: Remote Sensing of Environment, v. 110, p. 287–303.

Scott, K.M. and Yang, K., 1997, Spectral reflectance studies of white micas: Exploration and mining report 439R. CSIRO Division of Exploration and Mining, Australia, 35 p.

Settle, J.J. and Drake, N.A., 1993, Linear mixing and the estimation of ground cover proportions: International Journal of Remote Sensing, v. 14, p. 1159-1177.

Shepard, D., 1968, A two-dimensional interpolation function for irregularly-spaced data: Proceedings of the 1968 ACM (Association for Computing Machinery) National Conference, New York, USA, p. 517–524.

Sims, D.A. and Gamon, J.A., 2002, Relationships between leaf pigment content and spectral reflectance across a wide range of species, leaf structures and developmental stages: Remote Sensing of Environment, v. 81, p. 337–354.

Swayze, G.A., Clark, R.N., Goetz, A.F.H., Chrien, T.G. and Gorelick, N.S., 2003, Effects of spectrometer band pass, sampling, and signal-to-noise ratio on spectral identification using the Tetracorder algorithm: Journal of Geophysical Research, v. 108, doi: 10.1029/2002JE001975.

Van Ruitenbeek, F.J.A., Cudahy, T., Hale, M. and van der Meer, F.D., 2005, Tracing fluid pathways in fossil hydrothermal systems with near-infrared spectroscopy: Geology, v. 33, p. 597–600.

Van Ruitenbeek, F.J.A., Debba, P., van der Meer, F. M., Cudahy, T., van der Meijde, M. and Hale, M., 2006, Mapping white micas and their absorption wavelengths using hyperspectral band ratios: Remote Sensing of Environment, v. 102, p. 211–222.

Velde, B., 1965, Phengite micas: Synthesis, stability, and natural occurrence: American Journal of Science, v. 263, p. 886-913.

Yang, K. and Huntington, J.F., 1996, Spectral signatures of hydrothermal

alteration in the metasediments at Dead Bullock Soak, Tatami desert, Northern Territory: Exploration and mining report 270R. CSIRO Division of Exploration and Mining, New South Wales, Australia, 29 p.

Yang, K., Huntington, J.F., Gemmell, J.B. and Scott, K.M., 2011, Variations in composition and abundance of white mica in the hydrothermal alteration system at Hellyer, Tasmania, as revealed by infrared reflectance spectroscopy: Journal of Geochemical Exploration, v. 108, p. 143–156.

**Fig. 1.** Geological map of the study area showing the locations of the ground spectrometry and sample collection sites. Also shown are the geographical locations of samples 51, 53, 54, 55, 56 and 59. The airborne survey covers the whole study area. Lithology and sulfide lenses GIS data from Minerals and Metals Group Ltd (unpubl.). The < 1% $Na_2O$ (in rock surface samples) isoline is modified from Morrison (2004). sp.=spectrometry.

**Fig. 2.** A) Typical undisturbed rhyolitic rock outcrop with lichen cover. B) Left half: undisturbed rhyolitic rock outcrop with lichen cover, and right half: spectral measurement being taken with contact probe from pressure-washed, rhyolitic rock outcrop.

**Fig. 3.** Photomicrographs of samples: A) 51; B) 53; C) 54; D) 55; E) 56; F) 59. All photomicrographs in plain polarized light.

**Fig. 4.** A) bivariate plot of the Fe-OH wavelength position (in nm) versus the Mg/(Mg+Fe) ratio of biotite/chlorite. B) bivariate plot of the Al-OH wavelength position (in nm) versus the Si/Al ratio of white micas. C) bivariate plot of the Al-OH wavelength position (in nm) versus the Mg+Fe content of white mica. All graphs are shown with a linear fit line.

**Fig. 5**. Ground spectrometry; A) histogram of the wavelength range of the hull quotient

corrected Fe-OH absorption features; B) 1: spectral measurement 50 (2259 nm), spectrum 2: spectral measurement 282 (2250 nm); C) hull quotient-corrected spectra 1 and 2. Spectra 1 and 2 represent the long (2259 nm) and the short (2250 nm) endmembers of the Fe-OH absorption feature wavelength positions of the ground spectrometry, respectively.

**Fig. 6**. Ground spectrometry; A) spatial distribution map of the Fe-OH wavelength position; B) bivariate plot of the Fe-OH absorption feature wavelength position versus distance to the nearest massive sulfide lens.

**Fig. 7.** Ground spectrometry; A) histogram of the wavelength range of the hull quotient-corrected Al-OH absorption features; B) 1: averaged spectral measurements 321-326 (2211 nm), spectrum 2: averaged spectral measurements 193-195 (2195 nm); C) hull quotient-corrected spectra 1 and 2. Spectra 1 and 2 represent the long (2211 nm) and the short (2195 nm) endmembers of the Al-OH absorption feature wavelength positions of the ground spectrometry, respectively.

**Fig. 8**. A) spatial distribution map of the Al-OH absorption feature wavelength positions extracted from the ground spectrometry; B) spatial distribution map of the 1$^{st}$ and 4$^{th}$ quartile ranges for the Al-OH absorption feature wavelengths extracted from the ground spectrometry.

**Fig. 9**. A) frequency distribution histogram of the Al-OH absorption features of the airborne spectrometry; B) frequency distribution histogram of the Al-OH absorption feature wavelengths extracted from ground spectrometry, re-sampled to the sampling interval of the airborne data.

**Fig. 10**: A) Spatial distribution map of the interpolated Al-OH absorption feature wavelengths extracted from the airborne data; B) spatial distribution map of the 4$^{th}$ quartile of the Al-OH absorption features extracted from the ground spectrometry (2207-2211 nm) and airborne spectrometry (2205-2206 nm). Also shown in figures A and B is

an area of altered rock that is characterized by relatively long Al-OH wavelength positions both in the ground and airborne spectra ("area of enhanced alteration"). Rhyolitic rock outcrops, sulfide lenses, and the outline of Izok Lake GIS data are from Minerals and Metals Group Ltd. (unpubl.).

**Fig. 11.** Ground and airborne spectra; A) 1: spectral measurement 267 (2208 nm), 2: spectral measurement 37 (2202 nm); B) hull quotient-corrected spectra 1 and 2 of Figure A; C) spectral measurements 267 (2206 nm, spectrum 1) and 37 (2200 nm, spectrum 2) shown in Figure A, resampled to the sampling interval of the airborne spectra; D) hull quotient-corrected spectra 1 and 2 of Figure C; E) Airborne spectra 1-4, representing the absorption features near 2194 nm (spectrum 1), 2200 nm (spectrum 4), 2206 nm (spectrum 2) and 2212 nm (spectrum 3); F) hull quotient-corrected spectra 1-4 of Figure E. The sampling interval of the spectra is denoted by "x" in Figures B, D and F.

**Table 1.** Thin section samples, their mineralogy and the presence of the Al-OH and Fe-OH absorption features.

**Table 2**. Average compositions of the samples per mineral and the average Al-OH and Fe-OH absorption feature wavelength positions; *n*=number of analyses per sample; biot.=biotite, chl.=chlorite.

Figure 1

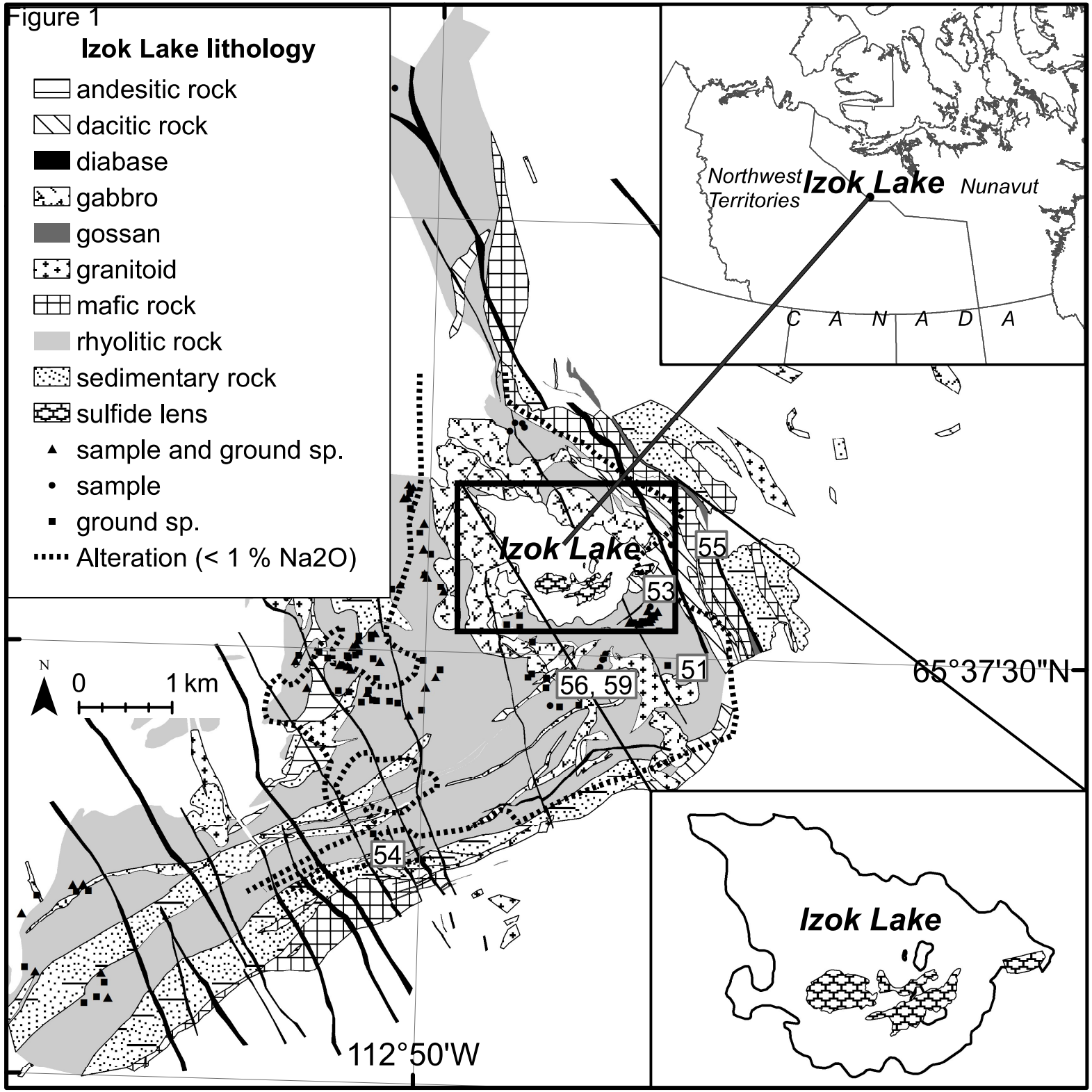
Izok Lake lithology
andesitic rock
dacitic rock
diabase
gabbro
gossan
granitoid
mafic rock
rhyolitic rock
sedimentary rock
sulfide lens
sample and ground sp.
sample
ground sp.
Alteration (< 1 % Na2O)
Northwest Territories
Izok Lake
Nunavut
C A N A D A
Izok Lake
55
53
51
56, 59
54
N
0
1 km
65°37'30"N
112°50'W
Izok Lake

Figure 2

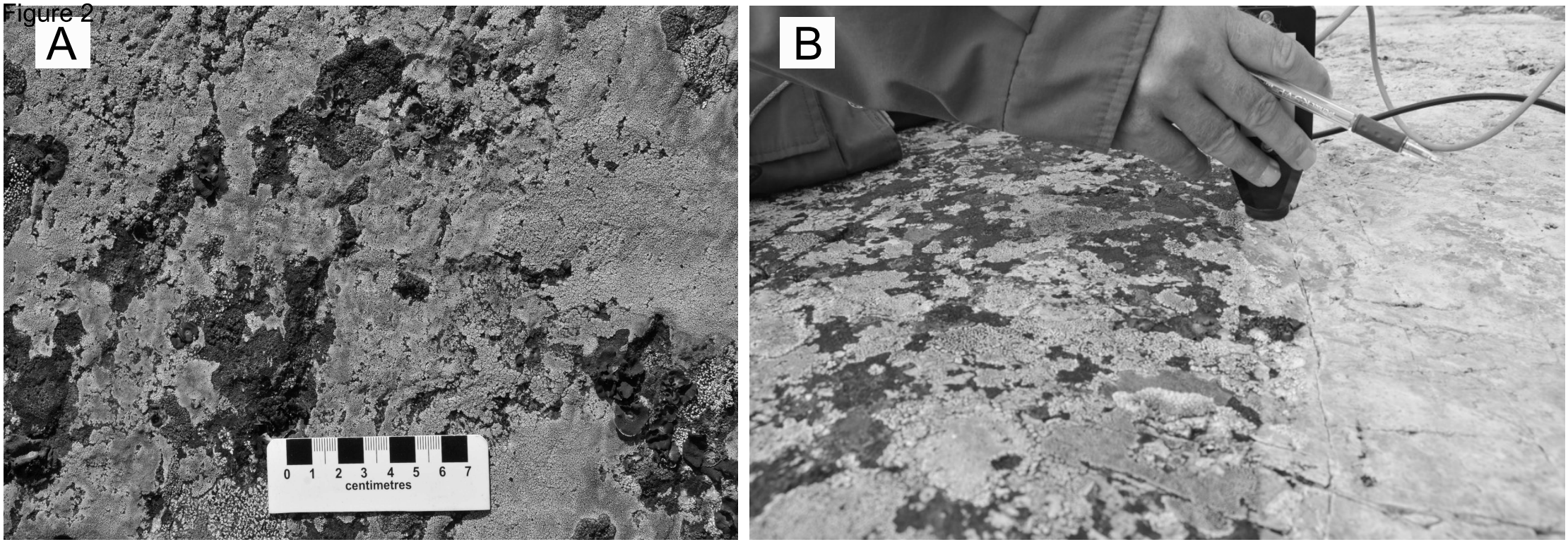

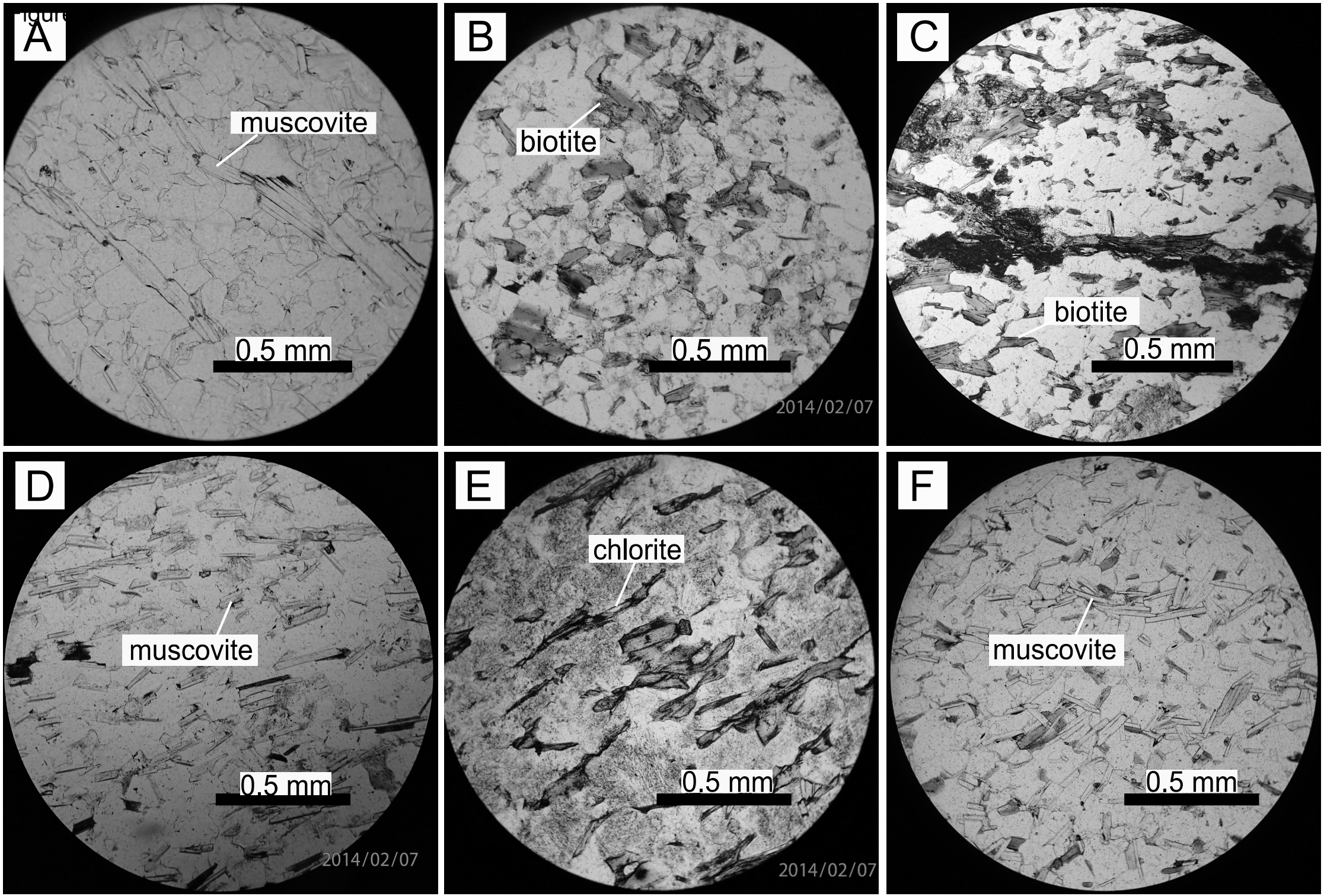
A
muscovite
0.5 mm
B
biotite
0.5 mm
2014/02/07
C
biotite
0.5 mm
D
muscovite
0.5 mm
2014/02/07
E
chlorite
0.5 mm
2014/02/07
F
muscovite
0.5 mm

Figure 4

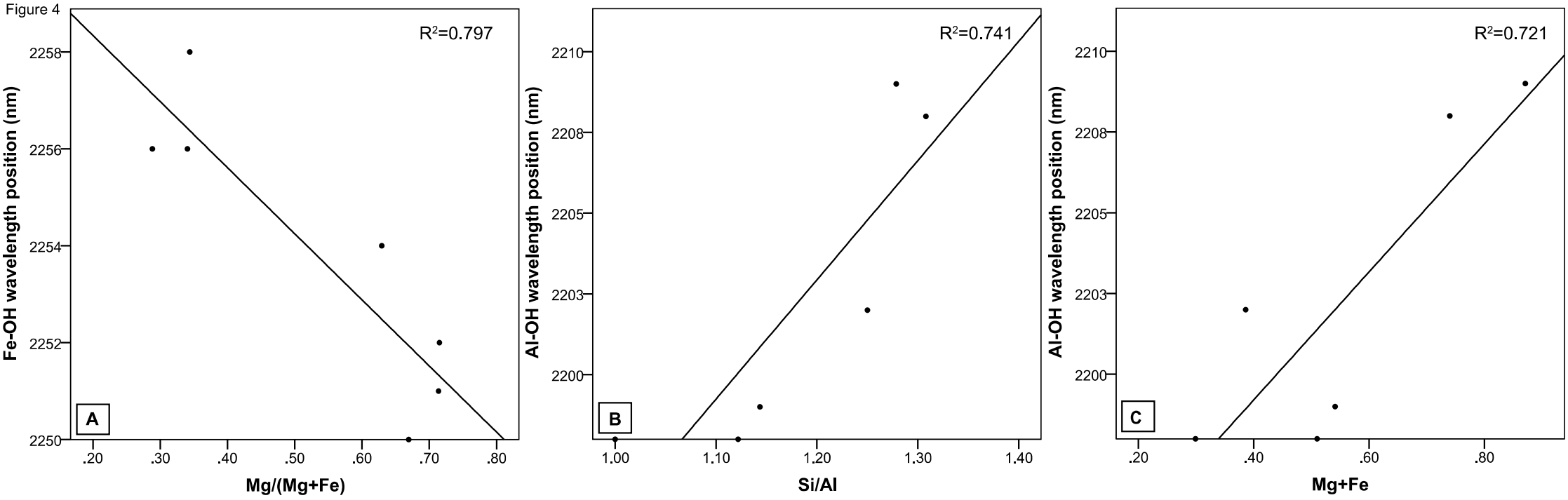
R²=0.797
Fe-OH wavelength position (nm)
2258
2256
2254
2252
2250
A
.20
.30
.40
.50
.60
.70
.80
Mg/(Mg+Fe)
R²=0.741
Al-OH wavelength position (nm)
2210
2208
2205
2203
2200
B
1.00
1.10
1.20
1.30
1.40
Si/Al
R²=0.721
Al-OH wavelength position (nm)
2210
2208
2205
2203
2200
C
.20
.40
.60
.80
Mg+Fe

Figure 5

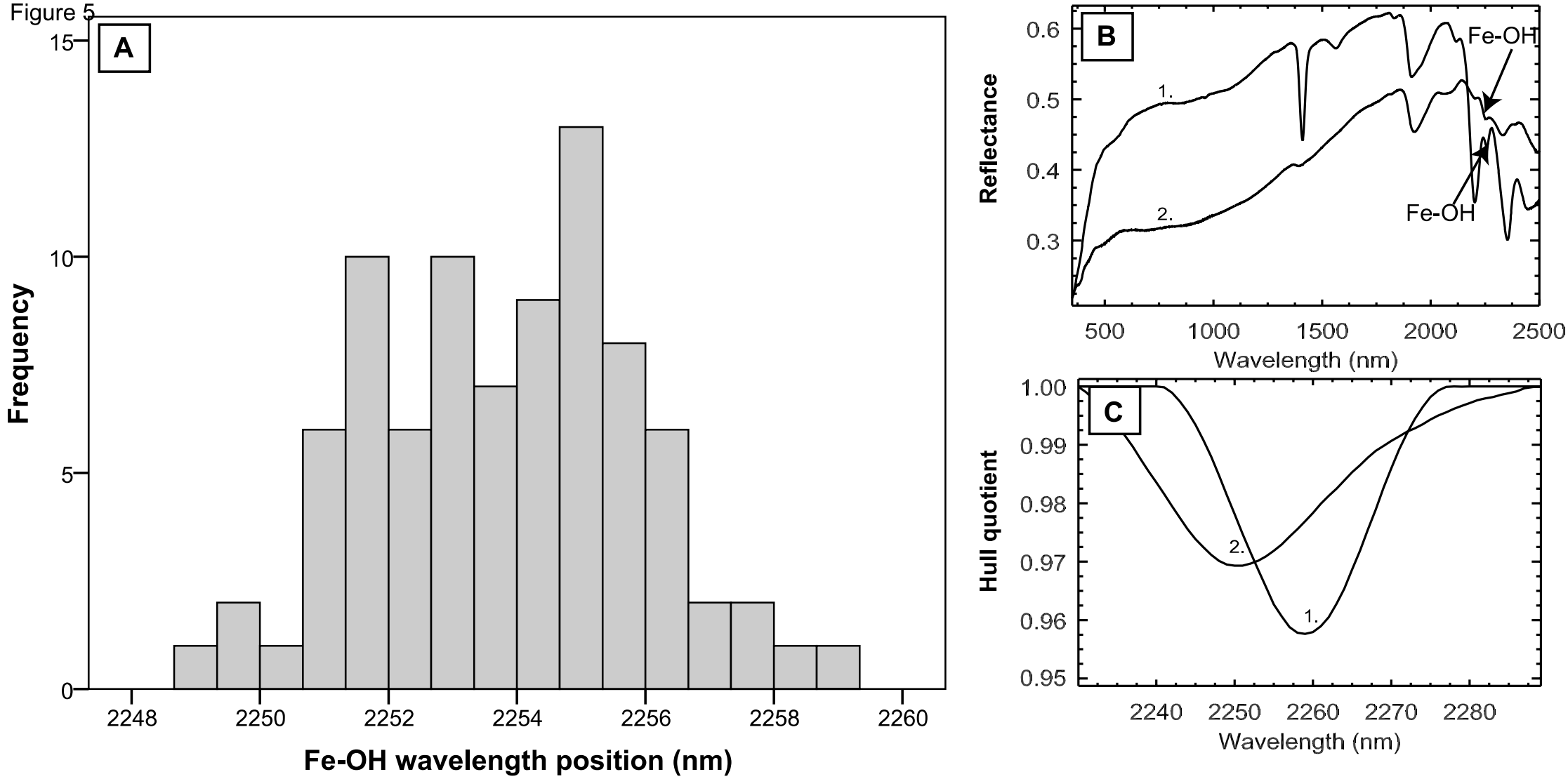
A
Frequency
Fe-OH wavelength position (nm)
0
5
10
15
2248
2250
2252
2254
2256
2258
2260
B
Reflectance
Wavelength (nm)
Fe-OH
Fe-OH
1.
2.
0.3
0.4
0.5
0.6
500
1000
1500
2000
2500
C
Hull quotient
Wavelength (nm)
1.
2.
0.95
0.96
0.97
0.98
0.99
1.00
2240
2250
2260
2270
2280

Figure 6

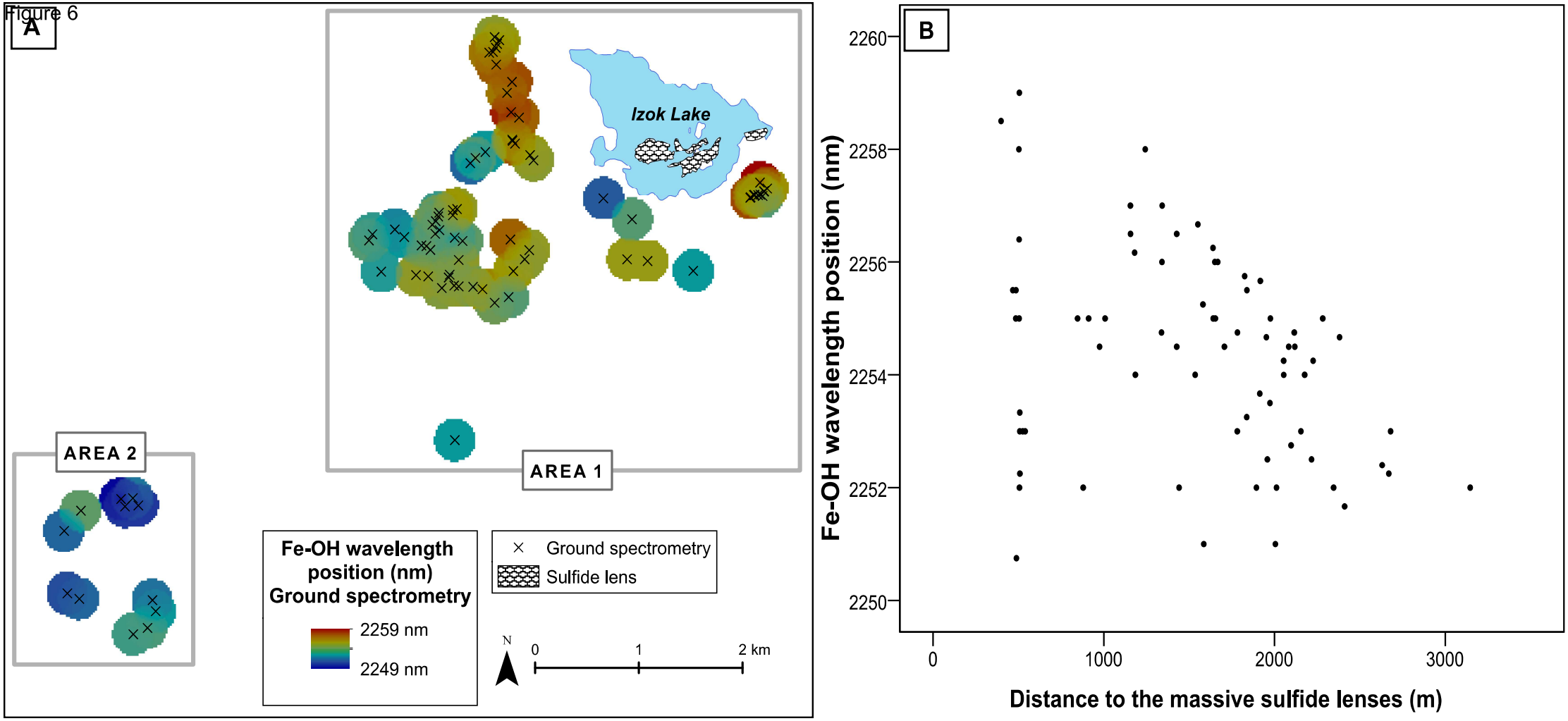
A
Izok Lake
AREA 1
AREA 2
Fe-OH wavelength position (nm) Ground spectrometry
2259 nm
2249 nm
Ground spectrometry
Sulfide lens
N
0
1
2 km
B
Fe-OH wavelength position (nm)
2260
2258
2256
2254
2252
2250
0
1000
2000
3000
Distance to the massive sulfide lenses (m)

Figure 7

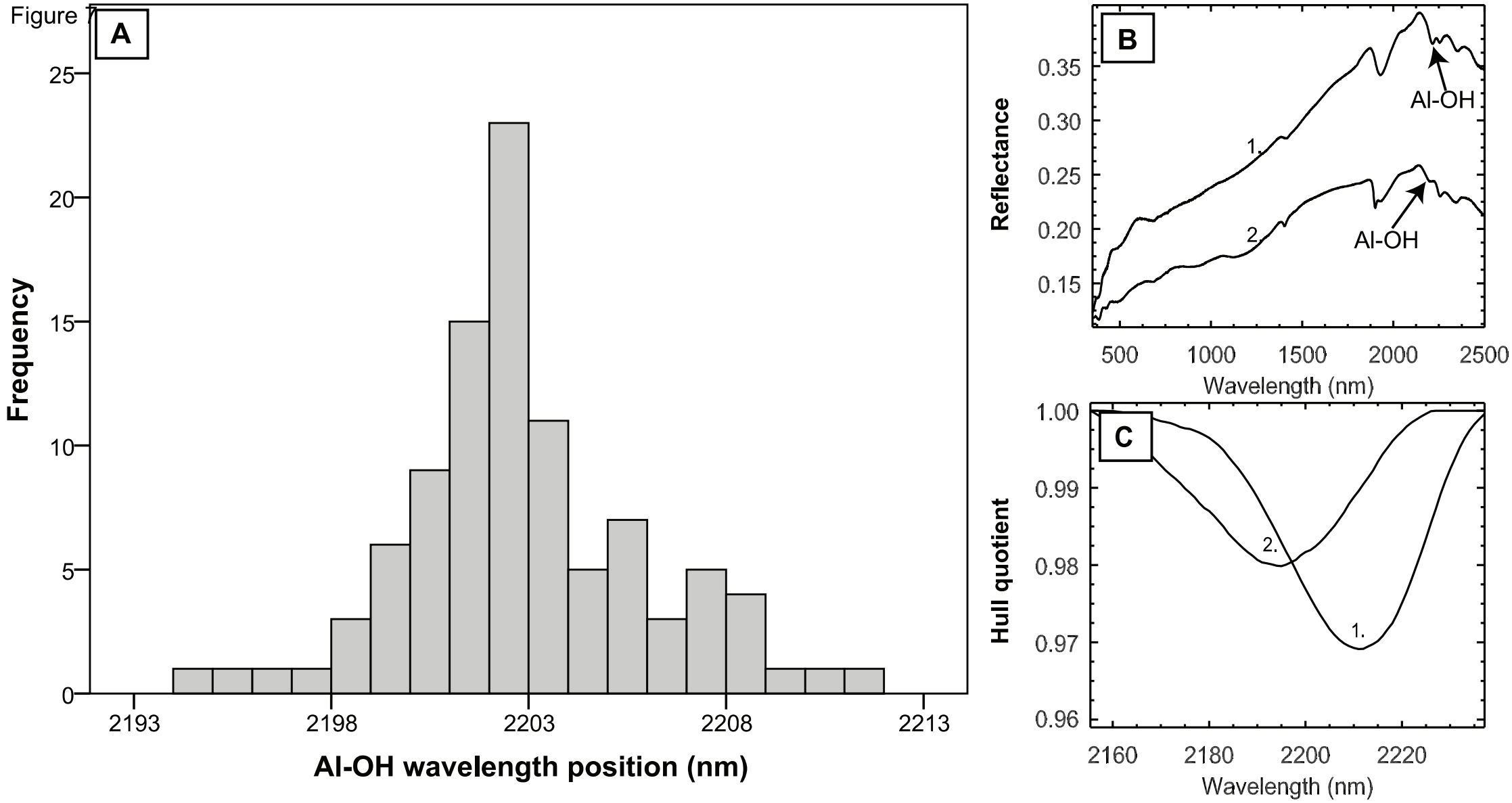
A
Frequency
0
5
10
15
20
25
2193
2198
2203
2208
2213
Al-OH wavelength position (nm)
B
Reflectance
0.15
0.20
0.25
0.30
0.35
500
1000
1500
2000
2500
Wavelength (nm)
1.
2.
Al-OH
Al-OH
C
Hull quotient
0.96
0.97
0.98
0.99
1.00
2160
2180
2200
2220
Wavelength (nm)
1.
2.

Figure 8

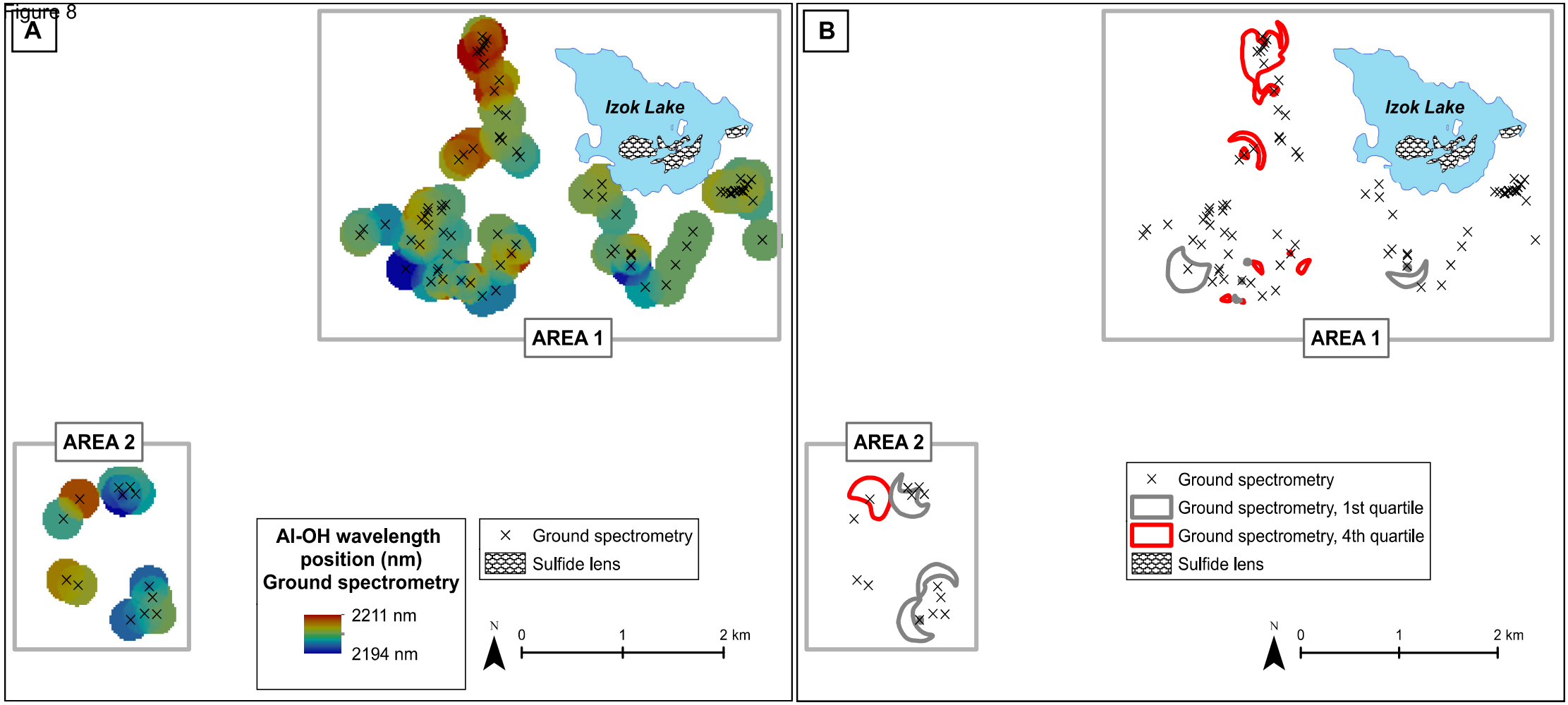
A
Izok Lake
AREA 1
AREA 2
Al-OH wavelength position (nm) Ground spectrometry
2211 nm
2194 nm
Ground spectrometry
Sulfide lens
N
0
1
2 km
B
Izok Lake
AREA 1
AREA 2
Ground spectrometry
Ground spectrometry, 1st quartile
Ground spectrometry, 4th quartile
Sulfide lens
N
0
1
2 km

Figure 9

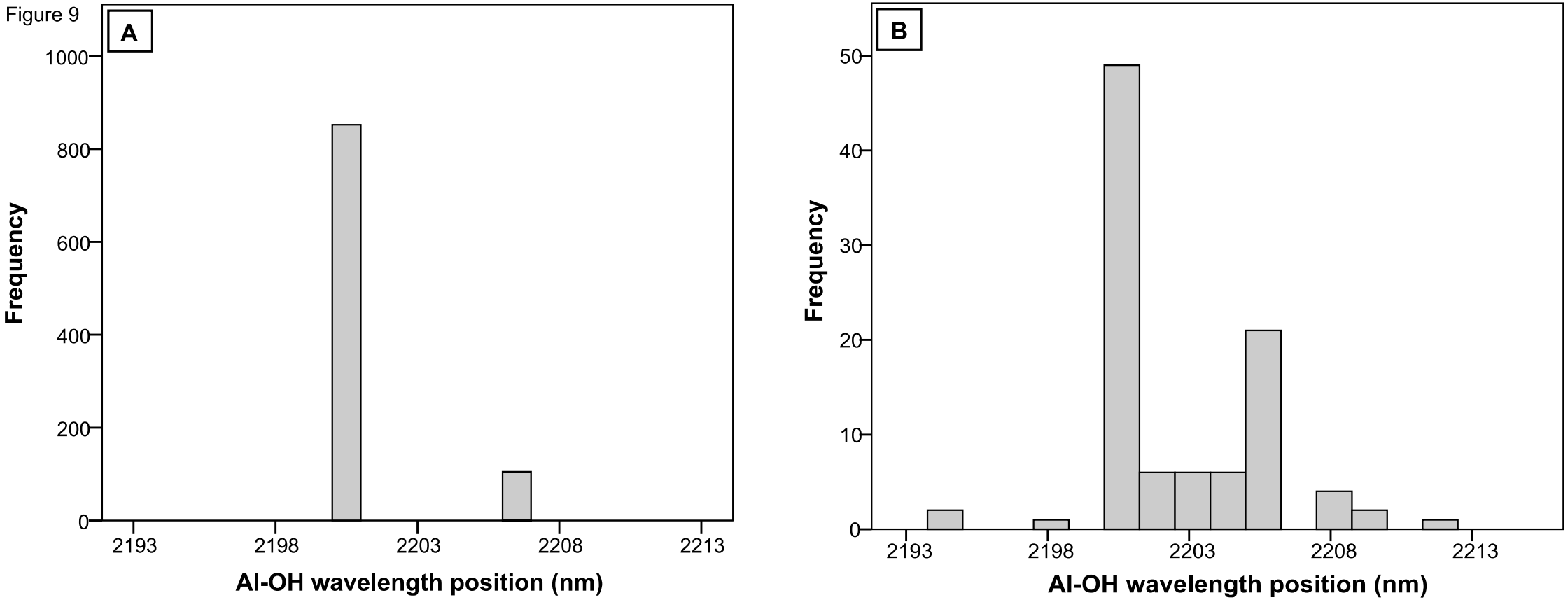
A
1000
800
600
400
200
0
Frequency
2193
2198
2203
2208
2213
Al-OH wavelength position (nm)
B
50
40
30
20
10
0
Frequency
2193
2198
2203
2208
2213
Al-OH wavelength position (nm)

Figure 10

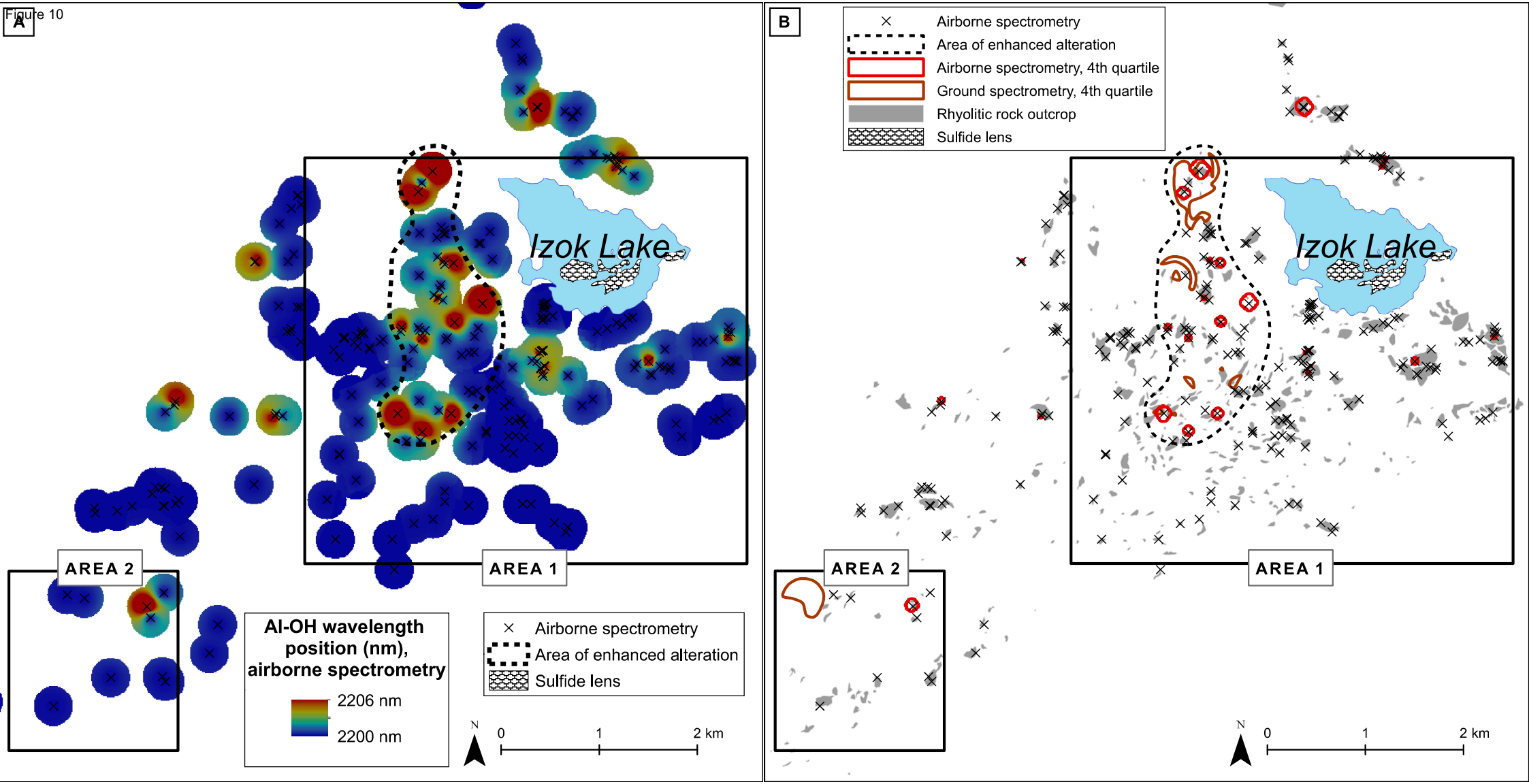
A
Izok Lake
AREA 1
AREA 2
Al-OH wavelength position (nm), airborne spectrometry
2206 nm
2200 nm
Airborne spectrometry
Area of enhanced alteration
Sulfide lens
N
0
1
2 km
B
Airborne spectrometry
Area of enhanced alteration
Airborne spectrometry, 4th quartile
Ground spectrometry, 4th quartile
Rhyolitic rock outcrop
Sulfide lens
Izok Lake
AREA 1
AREA 2
N
0
1
2 km

Figure 11

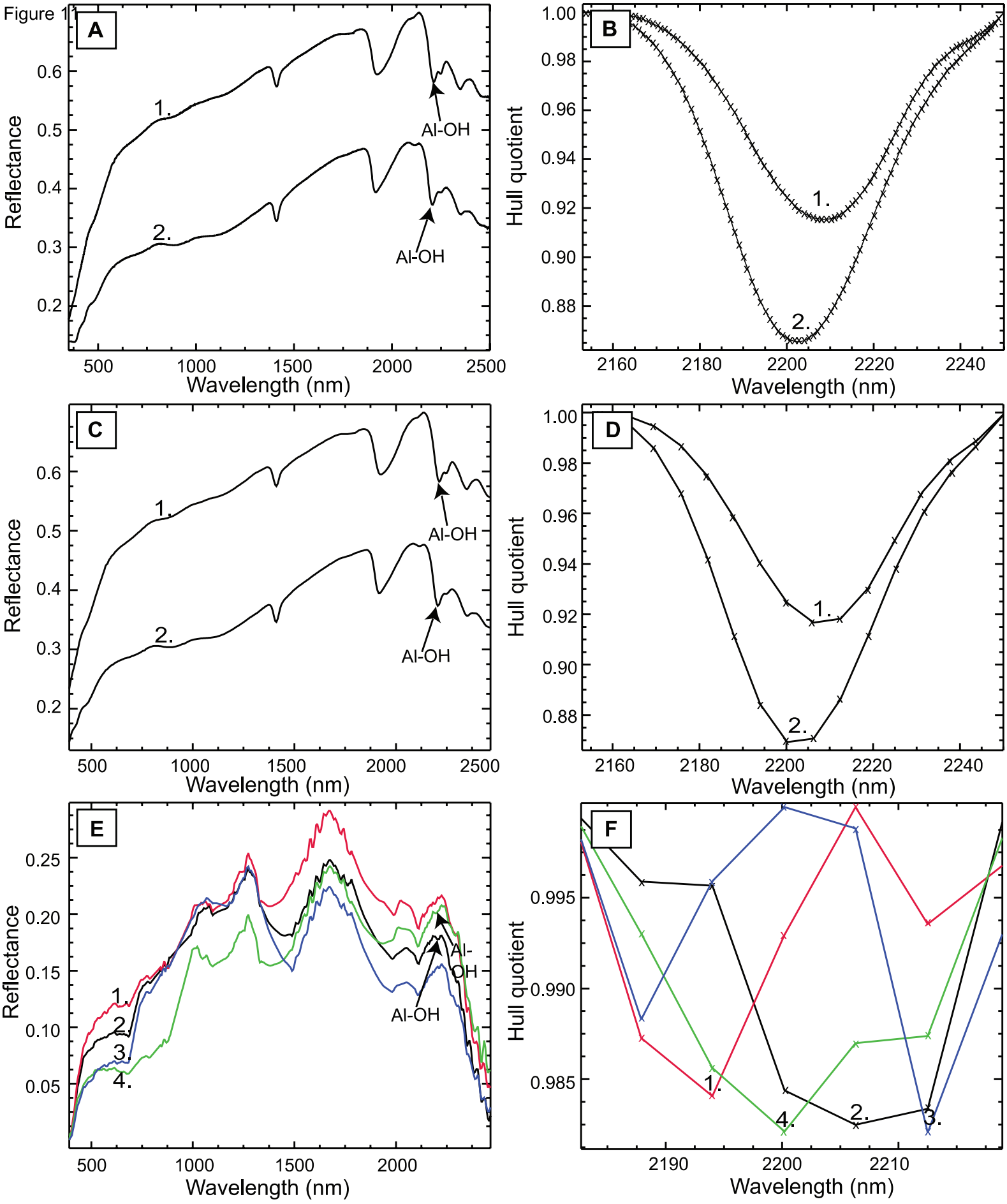
A
Reflectance
Wavelength (nm)
1.
2.
Al-OH
Al-OH
B
Hull quotient
Wavelength (nm)
1.
2.
C
Reflectance
Wavelength (nm)
1.
2.
Al-OH
Al-OH
D
Hull quotient
Wavelength (nm)
1.
2.
E
Reflectance
Wavelength (nm)
1.
2.
3.
4.
Al-OH
Al-OH
F
Hull quotient
Wavelength (nm)
1.
2.
3.
4.

Table 1

| Sample no. | biotite | chlorite | muscovite | Al-OH | Fe-OH |
|---|---|---|---|---|---|
| 51 | X | | X | X | X |
| 53 | X | | | X | X |
| 54 | X | | X | X | X |
| 55 | X | | X | X | X |
| 56 | | X | | | X |
| 59 | X | | X | X | X |

Table 2

| Sample no. | Al-OH (nm) | Fe-OH (nm) | Mineral | $Al_2O_3$ (wt%) | BaO (wt%) | CaO (wt%) | Cl (wt%) | F (wt%) | FeO (wt%) | $K_2O$ (wt%) | MgO (wt%) | MnO (wt%) | $Na_2O$ (wt%) | $SiO_2$ (wt%) | $TiO_2$ (wt%) | $V_2O_3$ (wt%) | Total |
|---|---|---|---|---|---|---|---|---|---|---|---|---|---|---|---|---|---|
| 27 | 2198 | 2254 | muscovite | 35.21 | 0.11 | 0.00 | 0.01 | 0.11 | 1.94 | 9.33 | 1.31 | 0.01 | 0.95 | 46.58 | 0.26 | 0.02 | 95.84 |
| ($n$ =70) | | | biot./chl. | 21.12 | 0.01 | 0.00 | 0.03 | 0.35 | 16.59 | 4.47 | 15.87 | 0.16 | 0.11 | 31.43 | 0.51 | 0.01 | 90.66 |
| 29 | | 2250 | muscovite | 29.23 | 0.24 | 1.32 | 0.00 | 0.24 | 1.96 | 9.82 | 2.83 | 0.02 | 0.68 | 48.72 | 0.47 | 0.02 | 95.55 |
| ($n$ =45) | | | biot./chl. | 18.15 | 0.09 | 1.11 | 0.01 | 0.69 | 13.94 | 4.78 | 16.57 | 0.10 | 0.35 | 35.26 | 0.87 | 0.02 | 91.94 |
| 31 | 2199 | 2251 | muscovite | 34.26 | 0.24 | 0.00 | 0.01 | 0.10 | 2.10 | 10.00 | 1.30 | 0.01 | 0.74 | 46.17 | 0.21 | 0.02 | 95.16 |
| ($n$ =38) | | | biot./chl. | 20.45 | 0.06 | 0.00 | 0.05 | 0.83 | 10.51 | 8.51 | 14.69 | 0.08 | 0.15 | 37.61 | 0.74 | 0.02 | 93.70 |
| 34 | 2209 | 2258 | muscovite | 31.21 | 0.32 | 0.00 | 0.00 | 0.22 | 4.33 | 10.71 | 1.53 | 0.06 | 0.20 | 47.03 | 0.43 | 0.02 | 96.06 |
| ($n$ =46) | | | biot./chl. | 18.24 | 0.06 | 0.01 | 0.03 | 0.22 | 26.51 | 5.61 | 7.84 | 0.68 | 0.10 | 31.31 | 0.96 | 0.01 | 91.58 |
| 35 | 2208 | 2256 | muscovite | 30.47 | 0.27 | 0.30 | 0.01 | 0.23 | 3.76 | 10.29 | 1.50 | 0.04 | 0.50 | 46.99 | 0.17 | 0.01 | 94.55 |
| ($n$ =59) | | | biot./chl. | 17.63 | 0.09 | 1.35 | 0.07 | 0.55 | 22.71 | 6.82 | 6.57 | 0.37 | 0.10 | 36.77 | 0.78 | 0.02 | 93.82 |
| 37 | 2202 | 2256 | muscovite | 31.96 | 0.08 | 0.00 | 0.00 | 0.10 | 2.95 | 11.35 | 0.44 | 0.02 | 0.39 | 47.37 | 0.25 | 0.01 | 94.92 |
| ($n$ =55) | | | biot./chl. | 18.73 | 0.02 | 0.00 | 0.06 | 0.19 | 26.57 | 6.83 | 5.24 | 0.40 | 0.08 | 33.33 | 0.96 | 0.01 | 92.42 |
| 47 | 2198 | 2252 | muscovite | 35.04 | 0.05 | 0.00 | 0.00 | 0.04 | 0.88 | 10.91 | 1.00 | 0.01 | 0.37 | 46.13 | 0.15 | 0.01 | 94.59 |
| ($n$ =37) | | | biot./chl. | 20.56 | 0.01 | 0.00 | 0.02 | 0.29 | 11.68 | 7.69 | 16.39 | 0.05 | 0.08 | 35.38 | 0.53 | 0.01 | 92.69 |